AN ABSTRACT OF THE THESIS OF

Prajwal Prakash Adiga for the degree of Master of Science in Chemical Engineering presented on December 5, 2018.

Title: Hydraulic Jump Dynamics for Water Jet Impingement on Vertically Oriented Rotating Surfaces.

Abstract approved:

Willie E. "Skip" Rochefort

Silicon wafer cleaning is a ubiquitous unit operation in the semiconductor industry to remove excess material or nanoparticle impurities to obtain perfectly smooth and clean wafer surfaces. Extensive research has already been completed to understand the physics behind hydraulic jumps observed due to balance of forces when a coherent Newtonian or non-Newtonian jet impinges on a horizontal flat surface. With a need to clean surfaces that are vertically oriented such as industrial tanks and microelectronics processing equipment requiring a smaller "footprint", researchers have shifted attention towards understanding the physics behind hydraulics jumps (in some literature, also called the 'film jumps') when a coherent horizontal jet impinges on a vertical flat surface. With participating forces like gravity, momentum and surface tension anticipated to play a role in defining the shape and size of such hydraulic jumps, the current work attempts to include the role of centrifugal force to understand the phenomenological dynamics of the hydraulic jump at different rotational speeds. Silicon wafers of varying surface characteristics, as determined from contact angle

measurements, were studied and a summary of these observations will be presented. A phase diagram relating the Strouhal number (a function of rotational frequency) to the impinging jet Reynolds number has been developed to indicate regions where the hydraulic jump disappears.

©Copyright by Prajwal Prakash Adiga
December 5, 2018
All Rights Reserved

Title: Hydraulic Jump Dynamics for Water Jet Impingement on Vertically Oriented Rotating Surfaces

by

Prajwal Prakash Adiga

A THESIS

submitted to

Oregon State University

in partial fulfillment of

the requirements for the

degree of

Master of Science

Presented December 5, 2018
Commencement June 2019

Master of Science thesis of Prajwal Prakash Adiga, presented on December 5, 2018

APPROVED:

Major Professor, representing Chemical Engineering

Head of the School of Chemical, Biological and Environmental Engineering

Dean of the Graduate School

I understand that my thesis will become part of the permanent collection of Oregon State University libraries. My signature below authorizes release of my thesis to any reader upon request.

Prajwal Prakash Adiga, Author

ACKNOWLEDGEMENTS

I would like to express the deepest appreciation to my advisor, Dr. Skip Rochefort who took me on as his student when the tides were against me. His positive approach and vision for this project has helped me amass sufficient content for this project.

I would also like to express my regards to Dr. Travis Walker who had me working on his project and acted as a pseudo-advisor throughout my association with this project. It was his high expectations that kept pushing me to go that extra mile while working on the project.

I would also like to thank my committee members, Dr. Chih Hung Chang and Dr. Ganti Murthy for supporting me through this journey of working towards a Masters degree.

A special section of my acknowledgements is dedicated to the senior lab team (John Cochran, Andy Brickman, Dr. Phil Harding and Dr. Trevor Carlisle) who, in some way or other helped me in finding the required hardware for my project and pitched in with advice when I needed one.

I would also like to show my gratitude to Aaron Nibler and all of the other undergraduates who industriously ran the experiments or were involved in shaping up this project.

My acknowledgements would be incomplete without my families (and I am lucky to have two), one in India (my dad - Prakash Adiga, my mom - Padma Adiga, my sister - Prajna, my brother-in-law - Pramod and my two nieces) and one in the US (Stanley Nudelman and Charla Van Koten), who have been influential in shaping up my personality and attitude towards life. I would also like to extend my gratitude towards my friends who have given me the moral support throughout my journey in life.

Lastly, I would like to thank School of Chemical, Biological and Environmental Engineering who kept me funded throughout my Masters and has provided me facilities and tools to succeed at school.

TABLE OF CONTENTS

Page

1. Introduction 1

2. Literature Review 3

3. Materials and Methods 5

4. Results 10

4.1. Coherent jet analysis 10
4.2. Water jet impingement on vertically oriented non-spinning silicon wafer 11
4.3. Water jet impingement on vertically oriented spinning "as-received" silicon wafers 19
4.3.1. Rotation of "as-received" 200 mm rough silicon wafer 20
4.3.2. Rotation of "as-received" 165 mm smooth silicon wafer 26
4.3.3. Rotation of "as-received" 300 mm smooth silicon wafer 30
4.4. Surface characterization by contact angle 36
4.5. Radio Corporation of America (RCA) Cleaning Process 42
4.6. Atomic Force Microscopy (AFM) 47
4.7. Water impingement on vertically oriented spinning cleaned silicon wafer 51
4.7.1. Rotation of cleaned 200 mm rough silicon wafer 51
4.7.2. Rotation of cleaned 165 mm smooth silicon wafer 55
4.8. Wafer draining test 58
4.9. Phase Diagram 61

5. Discussion and Future Work 63

6. Nomenclature 66

7. References 67

Appendix A 69
Appendix B 72

LIST OF FIGURES

Figure Page

Figure 1: Water jet impingement on vertically oriented stationary surface................. 2

Figure 2: Front view of a post-CMP rinsing device developed by Applied materials®. 5

Figure 3: Section A-A (plan view) and rear view of the post-CMP rinsing device...... 5

Figure 4: A simplified view of the CMP machine representing a wafer pad, a nozzle and a DC drive quintessential for impinging water jets on rotating wafer. 6

Figure 5: A detailed process flow diagram (PFD) of the system................................ 8

Figure 6: Experimental setup of the system.. 9

Figure 7: Capillary-driven instability of a water jet under the influence of gravity oriented in a horizontal direction. 10

Figure 8: Observed shape of a hydraulic jump on vertical surface with nomenclatures used to quantitatively qualify hydraulic jump. 11

Figure 9: Schematic of hydraulic jump observed during jet impingement on a vertically oriented surface... 12

Figure 10: Pictorial representation of slack in the jet path observed low flow rates (< 0.2 USGPM) for 4 m diameter jet.. 12

Figure 11: Non-dimensionalized inner height of hydraulic jump (parallel to gravity) plotted against jet Reynolds number exhibits linear trend for varying jet diameter... 13

Figure 12: Non-dimensionalized outer height of hydraulic jump (parallel to gravity) plotted against jet Reynolds number exhibits linear trend for varying jet diameter... 13

Figure 13: Non-dimensionalized inner width of hydraulic jump (perpendicular to gravity) plotted against jet Reynolds number exhibits linear trend for varying jet diameter.. 14

Figure 14: Non-dimensionalized outer width of hydraulic jump (perpendicular to gravity) plotted against jet Reynolds number exhibits linear trend for varying jet diameter.. 14

Figure 15: Non-dimensionalized thickness of hydraulic jump (parallel to gravity) plotted against jet Reynolds number... 15

Figure 16: Non-dimensionalized thickness of hydraulic jump (perpendicular to gravity) plotted against jet Reynolds number. 15

Figure 17: Non-dimensionalized inner width of hydraulic jump (perpendicular to gravity) plotted against jet Reynolds number for a 2 mm nozzle. Trends show a good match with experimental data run by Wang et al. (2013). 16

Figure 18: Non-dimensionalized inner width of hydraulic jump (perpendicular to gravity) plotted against jet Reynolds number for a 3 mm nozzle. Trends show a good match with experimental data run by Wang et al. (2013). 16

Figure 19: Non-dimensionalized inner width of hydraulic jump (perpendicular to gravity) plotted against jet Reynolds number for a 4 mm nozzle. Trends show a good match with experimental data run by Wang et al. (2013). 17

Figure 20: Non-dimensionalized outer width of hydraulic jump (perpendicular to gravity) plotted against non-dimensionalized inner width of hydraulic jump (perpendicular to gravity) superimposed over experimental data by Wang et al. (2013). 17

Figure 21: Rotation of "as-received" 200 mm rough silicon wafer in clockwise direction causing change in the shape of the hydraulic jump. 19

Figure 22: Slacking of jets in the coherent length of the jet under the influence of gravity. 20

Figure 23: Still image of an "as-received" rough silicon wafer of diameter 200 mm. 20

Figure 24: Eddies observed at relatively low rotational speeds (bracketed between 35 RPM and 50 RPM). The still image is at a flowrate of 0.4 USGPM and a rotational speed of 45 RPM. 21

Figure 25: Secondary hydraulic jump observed at relatively rotational speeds over 50 RPM. The still image is at a flowrate of 0.4 USGPM and a rotational speed of 62 RPM. 21

Figure 26: Ripples observed at rotational speeds that seemed to be a function of flowrate. The still image is for an "as-received" 200 mm rough wafer at a flowrate of 0.4 USGPM and a rotational speed of 121 RPM. 22

Figure 27: Image matrix (part-1) for an "as-received" 200 mm rough silicon wafer at different rotational speeds when impinging coherent water jet at a flowrate of 0.4 USGPM. 23

Figure 28: Image matrix (part-2) for an "as-received" 200 mm rough silicon wafer at different rotational speeds when impinging coherent water jet at a flowrate of 0.4 USGPM. 24

Figure 29: Disappearance of hydraulic jump for an “as-received” 200 mm rough silicon wafer at 243 RPM when impinging coherent water jet at a flowrate of 0.4 USGPM. The time-scale ($t_1 \rightarrow t_8$) at critical rotational speed for disappearance of hydraulic jump is bracketed between 3 – 5 seconds. 25

Figure 30: Still image of an “as-received” smooth silicon wafer of diameter 165 mm. 26

Figure 31: Sticking phenomena on an “as-received” 165 mm smooth silicon wafer. 26

Figure 32: Slipping phenomena on an “as-received” 165 mm smooth silicon wafer. 27

Figure 33: Ripples observed at rotational speeds that seemed to be a function of flowrate. The still image is for an “as-received” 165 mm smooth silicon wafer at a flowrate of 0.4 USGPM and a rotational speed of 131 RPM. 27

Figure 34: Image matrix for an “as-received” 165 mm smooth silicon wafer at different rotational speeds when impinging coherent water jet at a flowrate of 0.4 USGPM. 28

Figure 35: Image matrix for an “as-received” 165 mm smooth silicon wafer at different rotational speeds when impinging coherent water jet at a flowrate of 0.4 USGPM. Disappearance of hydraulic jump was captured at 245 RPM. . The time-scale ($t_1 \rightarrow t_5$) at critical rotational speed for disappearance of hydraulic jump is bracketed between 3 - 5 seconds. 29

Figure 36: Still image of an “as-received” smooth silicon wafer of diameter 165 mm. 30

Figure 37: Eddies observed at low rotational speeds. The still image is at a flowrate of 0.4 USGPM and a rotational speed of 30 RPM. 30

Figure 38: Eddies transition into a secondary hydraulic jump. The still image is at a flowrate of 0.4 USGPM and a rotational speed of 44 RPM. 31

Figure 39: Ripples observed at rotational speeds that seemed to be a function of flowrate. The still image is for an as-received 300 mm smooth wafer at a flowrate of 0.4 USGPM and a rotational speed of 110 RPM. 31

Figure 40: Image matrix (part-1) for an “as-received” 300 mm smooth silicon wafer at different rotational speeds when impinging coherent water jet is at a flowrate of 0.4 USGPM. 33

Figure 41: Image matrix (part-2) for an “as-received” 300 mm smooth silicon wafer at different rotational speeds when impinging coherent water jet is at a flowrate of 0.4 USGPM. 34

Figure 42: Disappearance of hydraulic jump for an "as-received" 300 mm smooth silicon wafer at 272 RPM when impinging coherent water jet is at a flowrate of 0.4 USGPM. The time-scale ($t_1 \rightarrow t_8$) at critical rotational speed for disappearance of hydraulic jump is bracketed between 3 - 5 seconds. 35

Figure 43: Illustration of different behaviors that a liquid drop can exhibit on a solid surface. 36

Figure 44: Wafer alignment on FTA-135 stand for measuring contact angle along marked diameter of the wafer along X and Y directions in a Cartesian coordinate system. 37

Figure 45: Three contact angle trials on rough Si wafer at Y +60 mm spot dropping 5 μL water droplet. 38

Figure 46: Three contact angle trials on smooth Si wafer at Y +60 mm spot dropping 5 μL water droplet. 38

Figure 47: Contact angle measurements as a function of radius of rough Si wafer surface (Wafer diameter = 200 mm). Water droplet size of 5 μL was used. Dotted horizontal line shows mean contact angle for all of the measured data which was estimated to be 65.5º ± 11.6º. 38

Figure 48: Contact angle measurements as a function of radius of rough Si wafer surface (Wafer diameter = 200 mm). Water droplet size of 10 μL was used. Dotted horizontal line shows mean contact angle for all of the measured data which was estimated to be 63.6º ± 6.5º. 39

Figure 49: Contact angle measurements as a function of radius of smooth Si wafer surface (Wafer diameter = 165 mm). Water droplet size of 5 μL was used. Dotted horizontal line shows mean contact angle for all of the measured data which was estimated to be 42.5º ± 1.3º. 39

Figure 50: Contact angle measurements as a function of radius of smooth Si wafer surface (Wafer diameter = 165 mm). Water droplet size of 10 μL was used. Dotted horizontal line shows mean contact angle for all of the measured data which was estimated to be 42º ± 1.9º. 39

Figure 51: Contact angle measurements as a function of increasing droplet volume on rough and smooth Si wafer surfaces. 40

Figure 52: Contact angle measurements as a function of radius of smooth Si wafer surface (Wafer diameter = 300 mm). Water droplet size of 10 μL was used. Dotted horizontal line shows mean contact angle for all of the measured data which was estimated to be 57.6º ± 1.9º. 40

Figure 53: Illustration of contact angles for an even and a rough surface. 41

Figure 54: Step 1 of the RCA wash for the 165 mm smooth wafer indicates the onset of removal of organic contaminants indicated by the intensity of bubble generation which eventually subdues over a span of 15 minutes. 42

Figure 55: Contact angle of the cleaned 165 mm smooth silicon wafer compared to the as-received smooth silicon wafer. 44

Figure 56: Contact angle of the cleaned 200 mm rough silicon wafer with respect to the as-received rough silicon wafer. 45

Figure 57: AFM images of "as-received" 165 mm smooth silicon wafer at locations 1 and 2 for a scan area of 10 µm x 10 µm. 48

Figure 58: AFM images of "as-received" 165 mm smooth silicon wafer at locations 1 and 2 for a scan area of 5 µm x 5 µm. 48

Figure 59: AFM images of "as-received" 165 mm smooth silicon wafer at locations 1 and 2 for a scan area of 1 µm x 1 µm. 48

Figure 60: AFM images of cleaned 165 mm smooth silicon wafer at locations 1 and 2 for a scan area of 10 µm x 10 µm. 49

Figure 61: AFM images of cleaned 165 mm smooth silicon wafer at locations 1 and 2 for a scan area of 5 µm x 5 µm. 49

Figure 62: AFM images of cleaned 165 mm smooth silicon wafer at locations 1 and 2 for a scan area of 1 µm x 1 µm. 49

Figure 63: Image matrix (part-1) for a cleaned 200 mm rough silicon wafer at different rotational speeds when impinging coherent water jet at a flowrate of 0.4 USGPM. 52

Figure 64: Image matrix (part-2) for a cleaned 200 mm rough silicon wafer at different rotational speeds when impinging coherent water jet at a flowrate of 0.4 USGPM. 53

Figure 65: Disappearance of hydraulic jump for a cleaned 200 mm rough silicon wafer at 229 RPM when impinging coherent water jet at a flowrate of 0.4 USGPM. The time-scale ($t_1 \rightarrow t_6$) at critical rotational speed for disappearance of hydraulic jump is bracketed between 3 – 5 seconds. 54

Figure 66: Image matrix (part-1) for a cleaned 165 mm smooth silicon wafer at different rotational speeds when impinging coherent water jet at a flowrate of 0.3 USGPM. 56

Figure 67: Image matrix (part-2) and hydraulic jump disappearance for a cleaned 165 smooth silicon wafer at different rotational speeds when impinging coherent water jet

at a flowrate of 0.3 USGPM. The time-scale ($t_1 \rightarrow t_6$) at critical rotational speed for disappearance of hydraulic jump is bracketed between 3 seconds to 5 seconds. 57

Figure 68: "Cleaned" 200 mm rough wafer (L) rotation and (R) draining. 59

Figure 69: "As-received" 200 mm rough wafer (L) rotation and (R) draining. 59

Figure 70: "As-received" 165 mm smooth wafer (L) rotation and (R) draining. 59

Figure 71: "Cleaned" 165 mm smooth wafer (L) rotation and (R) draining. 60

Figure 72: "As-received" 300 mm silicon wafer (A) rotation, (B) draining at t = 0 second after stopping the impingement and rotation and (C) water pullback at t = 2 seconds after stoppingthe impingement and rotation. 60

Figure 73: The phase diagram relating the critical rotational speed of wafer to the jet velocity for all wafers irrespective of surface finish or size. 62

Figure 74: CalQFlo Rotameter calibration. 69

Figure 75: Rotational speed calibration for a smooth silicon wafer (D = 165 mm) with respect to the voltage of the drive. 69

Figure 76: Rotational speed calibration for a rough silicon wafer (D = 200 mm) with respect to the voltage of the drive. 70

Figure 77: Rotational speed calibration for a smooth silicon wafer (D = 300 mm) with respect to the voltage of the drive. 71

LIST OF TABLES

Table Page

Table 1: Average contact angle values for “as-received” silicon wafers used in the experiment... 41

Table 2: Average contact angle values for "as-received" and cleaned silicon wafers.46

Table 3: Mean squared average of surface roughness for smooth silicon wafer. 50

1. Introduction

Silicon wafer cleaning is a ubiquitous unit operation in the semiconductor industry to remove excess material or nanoscale impurities to develop a perfectly flat wafer for adding the next layer of circuit features. Chemical – mechanical planarization (CMP) has been employed by chipmakers for long which involves polishing of the surface using chemicals and mechanical abrasion on rotating wafers to achieve efficient cleaning. This post-CMP rinsing follows the CMP process and plays an important role in ensuring removal of any nanoscale impurities as these impurities can potentially cause "dishing" where the soft materials are recessed below harder impurities. Such a rinsing process involves impingement of polymer solutions in either a horizontal or vertical orientation. Applied Materials® has developed a post-CMP rinsing device that cleans the silicon wafer using vertical configuration. The setup is further discussed in Section 3 of this document.

Jet impingement for surface cleaning is one of the proven cleaning mechanisms in semiconductor industry. Though, the mechanism of cleaning for a horizontal orientation of wafer has been studied and deciphered for years, the mechanism of cleaning for a vertical orientation of wafer requires further investigation. The process involves many forces acting along the plane of surface and is a function of orientation of surface orientation. For a vertically oriented surface, gravitational force counters surface momentum built along the surface due to jet impingement on the surface. The region where this balance occurs is marked by a phenomenon called hydraulic jump (or film jump) wherein a thick rope of liquid is formed around the impinging jet on the surface. Such a jump is characteristic of surface tension of the fluid causing the fluid to rise out of the surface. Cleaning is essentially achieved along the hydraulic jump due to drag and extensional forces while the cleaning within the circumference of the hydraulic jump occurs due to momentum forces along the surface originating from point of impingement leaving a dry area of wafer entrained with impurities.

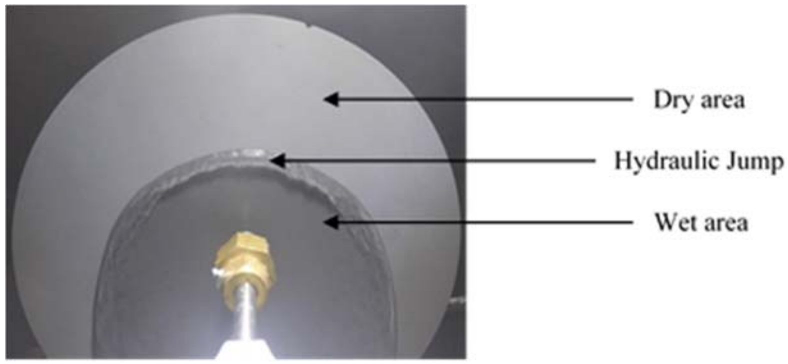

Figure 1: Water jet impingement on vertically oriented stationary surface.

The rotation of the wafer adds a new force to the existing dynamics observed along the surface. This can involve hydraulic jump transitions and additional phenomenological events that can eventually result in change of cleaning mechanisms along the surface of the wafer. Such a configuration is yet to be explored including events involving change of surface characteristics.

This study attempts to provide insight on the phenomenological dynamics of the hydraulic jump at different rotational speeds on a vertically oriented surface. Silicon wafers of varying surface characteristics – as determined from contact angle measurements – were studied and a summary of these observations are presented. Finally, a phase diagram relating the Strouhal number (a function of rotational frequency) to the impinging jet Reynolds number has been developed to indicate regions where the hydraulic jump disappears.

2. Literature Review

An extensive research has been accomplished to understand physics behind hydraulic jumps observed due to balance of forces when a coherent Newtonian and non-Newtonian jet impinges on horizontal flat surface. Such a configuration takes out gravity's contribution when a force balance is carried out on the surface.

For a stationary horizontal surface, Rayleigh (1914) used inviscid theory as basis for predicting the hydraulic jump radius. Tani (1949) accounted for the viscous effects followed by Watson (1964) who developed an appropriate description of the boundary layer that develops from the lower boundary accounting for the fluid viscosity on hydraulic jump radius. Watson (1964) studied both the radial and planar jet spreads for steady laminar and turbulent flows on a stationary solid surface. Watson's thin-film approach became the basis for numerous theoretical and experimental studies. Enhanced particle removal using viscoelastic fluids was studied by Walker et al. (2014). As rotating wafers pose a new dimension in understanding fluid mechanics of hydraulic jumps, rotation of horizontally oriented surface has been explored by Wang et al. (2018) theoretically and backed by measurements involving spin coaters.

With a need to clean surfaces that are vertically oriented like industrial tanks and facilities demanding less floor space, attention has been shifted towards understanding physics behind hydraulics jumps (in some literatures, also called the 'film jumps') when a coherent Newtonian jet impinges on a vertical flat surface. With participating forces like gravity and momentum anticipated to play role in defining the shape and size of such hydraulic jumps and surface effects altering these profiles, outcomes have been inconclusive on surface dependence over width and height of hydraulic jump. Primarily, polymethylmethacrylate (PMMA) and glass surfaces have been looked into in order to understand how surface plays out in defining shape and size of hydraulic jumps.

Morison et al. (2002) studied wetting of vertically oriented acrylic and stainless-steel surface using spray balls. Kibar et al. (2010) analyzed the physics of water jet impingements onto vertically oriented superhydrophobic surfaces. Attempts were made to correlate contact angle to jet inclination angle and Reynolds and Weber number. Wilson et al. (2011) investigated surface wetting behavior of spray ball jets and developed a simple model for the radial flow region based on momentum balances which validated Morison et al. (2002) experimental data and gave good predictions of flow region dimensions in experimental studies performed with water on glass and Perspex at low flow rates. This area of research has then pursued more or less by the same research group. The previously proposed model was modified by Wang et al. (2013) to account for the effect of gravity and the angle of inclination for non-horizontal jets. The location and flow pattern of the hydraulic jump around the impingement point was understood to be sensitive to the nature of substrate at low flow rates but insensitive to substrate nature at higher flow rates. Further, tendency to form dry patch within the falling film was predicted by a simple two-stream model. Bhagat et al. (2017) studied cleaning of tank and vessels and validated model proposed by Wilson et al. (2014) for adhesive removal of soiling layers by impinging coherent water jets. Inclined jet impingement was also investigated, and a new analysis was presented for calculating shape of the region cleared by the jet (which can be related to the hydraulic jump shape). One of the areas that has not been explored yet is coherent jet impingement on a vertically oriented rotating surface. This configuration finds application in a device used for rinsing silicon wafers post-CMP process.

Pierre-Gilles de Gennes (2004), in his book, “Capillarity and Wetting Phenomena” explained the effect of surface roughness on contact angle. Effect of increasing roughness of surface on advancing and receding contact angle on wax surfaces were presented. Surface roughness effects on fluid-substrate interactions can be helpful in analyzing surface coverage and eventually be tied in to cleaning efficiencies.

3. Materials and Methods

Post-Chemical mechanical planarization (CMP) rinsing device by Applied Materials® is used to planarize a surface at various stages in microchip manufacturing. The device has a spinning disc on which the wafer can be located. A slight vacuum ensures that the wafer stays attached to the disc even at high rotational speeds. A header conveying polymer solution is branched off ahead of the disc and nozzles located on these branches spray these solutions on the surface of the wafer. A hydraulically operated stem extends a disc that polishes the wafer.

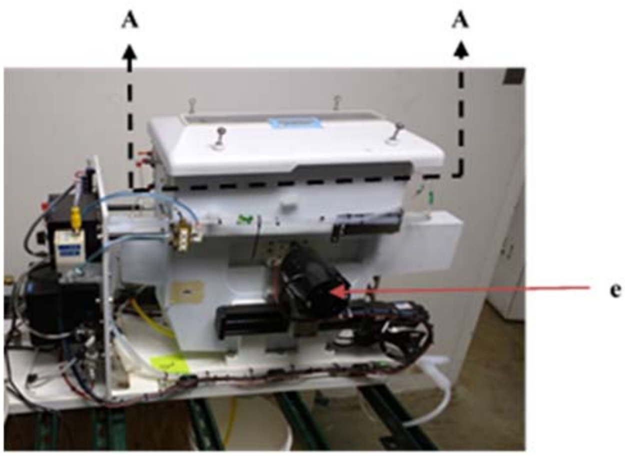

Figure 2: Front view of a post-CMP rinsing device developed by Applied materials®.

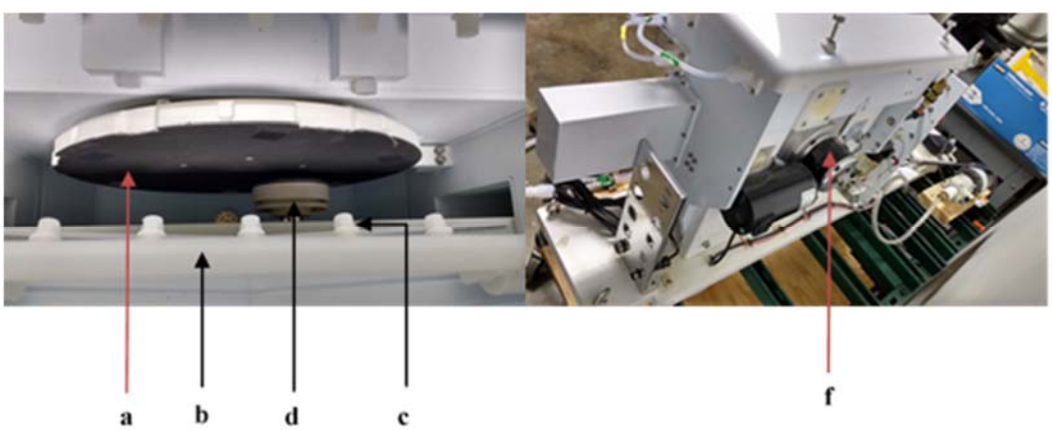

Figure 3: Section A-A (plan view) and rear view of the post-CMP rinsing device.

Figure 2 shows the drive [**e**] for the mechanical cleaning brush that can be viewed from the front view. The setup houses a wafer pad [**a**], distribution header [**b**], spray nozzles [**c**] and a mechanical cleaning brush [**d**] as seen in Figure 3. The drive [**f**] for the rotating the wafer pad is mounted at the rear side of the rinsing device.

The above system was simplified to focus only on the impingement of coherent jets on a rotational wafer. The multi nozzle header in CMP device was simplified in the basic experimental setup by using three nozzle sizes (2 mm, 3 mm, and 4 mm diameter). A peristaltic pump (MasterFlex I/P Model No. 77601-10) was used to impinge water jets through the nozzles. A suction tank (15 L capacity) with a continuous source of water supplied water to the pump. As pulsating flows were observed while pumping, a pulsation dampener (MasterFlex L/S Model No. 07596-20) was installed that helped avoid pulsations in the system. A CalQFlow rotameter (0 – 2.0 USGPM) was installed in the loop to record flow rates and the flow rate was adjusted through speed settings available on the peristaltic pump. The rotameter was calibrated for the entire flow range used as part of the study. The nozzle was secured on a jack which could roll on a roller to change the nozzle to wafer distance. The 3D printed spinning disc used in

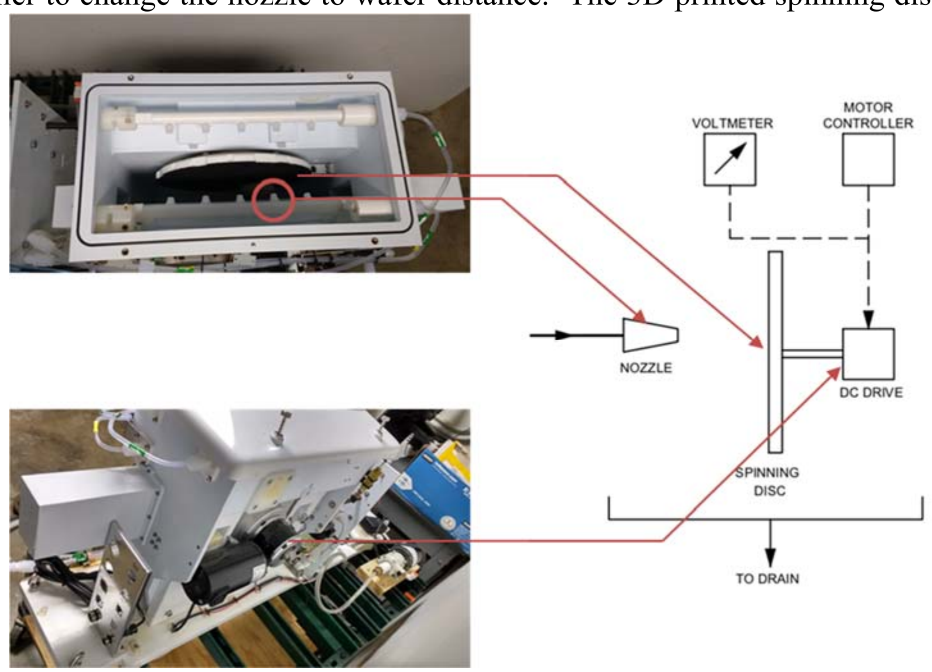

Figure 4: A simplified view of the CMP machine representing a wafer pad, a nozzle and a DC drive quintessential for impinging water jets on rotating wafer.

the system was connected to a DC drive (Bodine Electric Co. Type NSH-1105) with drive voltage controlled using a drive controller (Minarik Electric Co. Model No. SH-14). The nozzle and the disc were leveled off to ensure that the jet impinges perpendicular to the surface. Wafers with different surface characteristics were secured on the spinning disc and studied as part of the conducted experiments. Two "as-received" smooth silicon wafers; one with a diameter of 165 mm and the other with a diameter of 300 mm were impinged with water. The 165 mm smooth wafer was chemically cleaned (using RCA process) and impinged with water again to understand changes in hydraulic jump behaviors. A rough silicon wafer with diameter of 200 mm (both, as-received and RCA cleaned) was tested. The process flow diagram of the setup is shown in Figure 5.

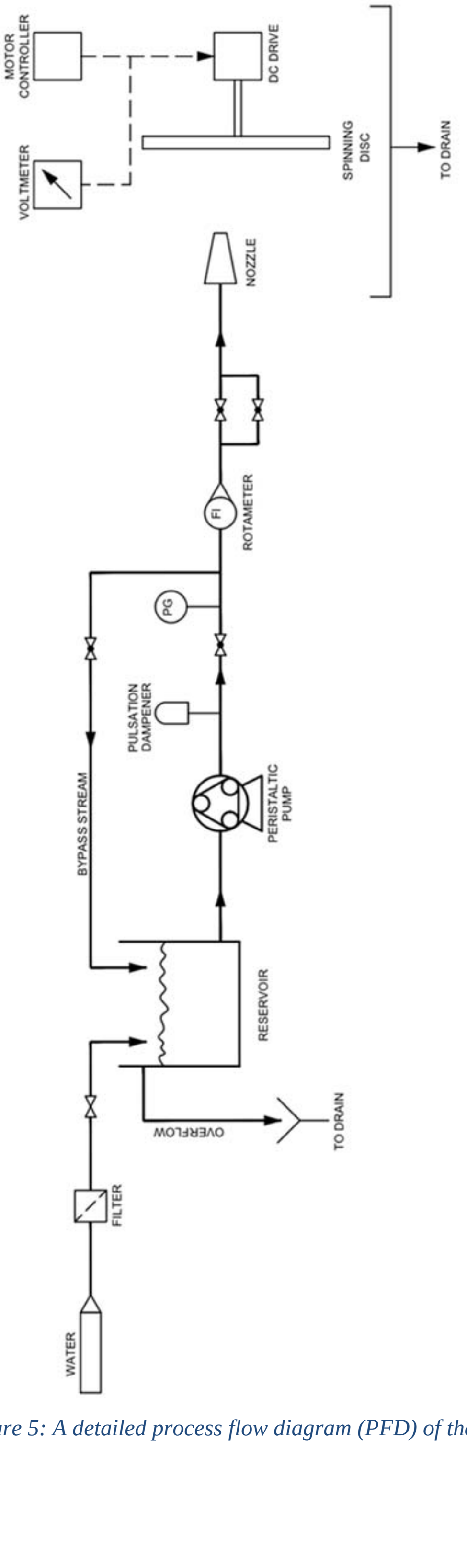

Figure 5: A detailed process flow diagram (PFD) of the system.

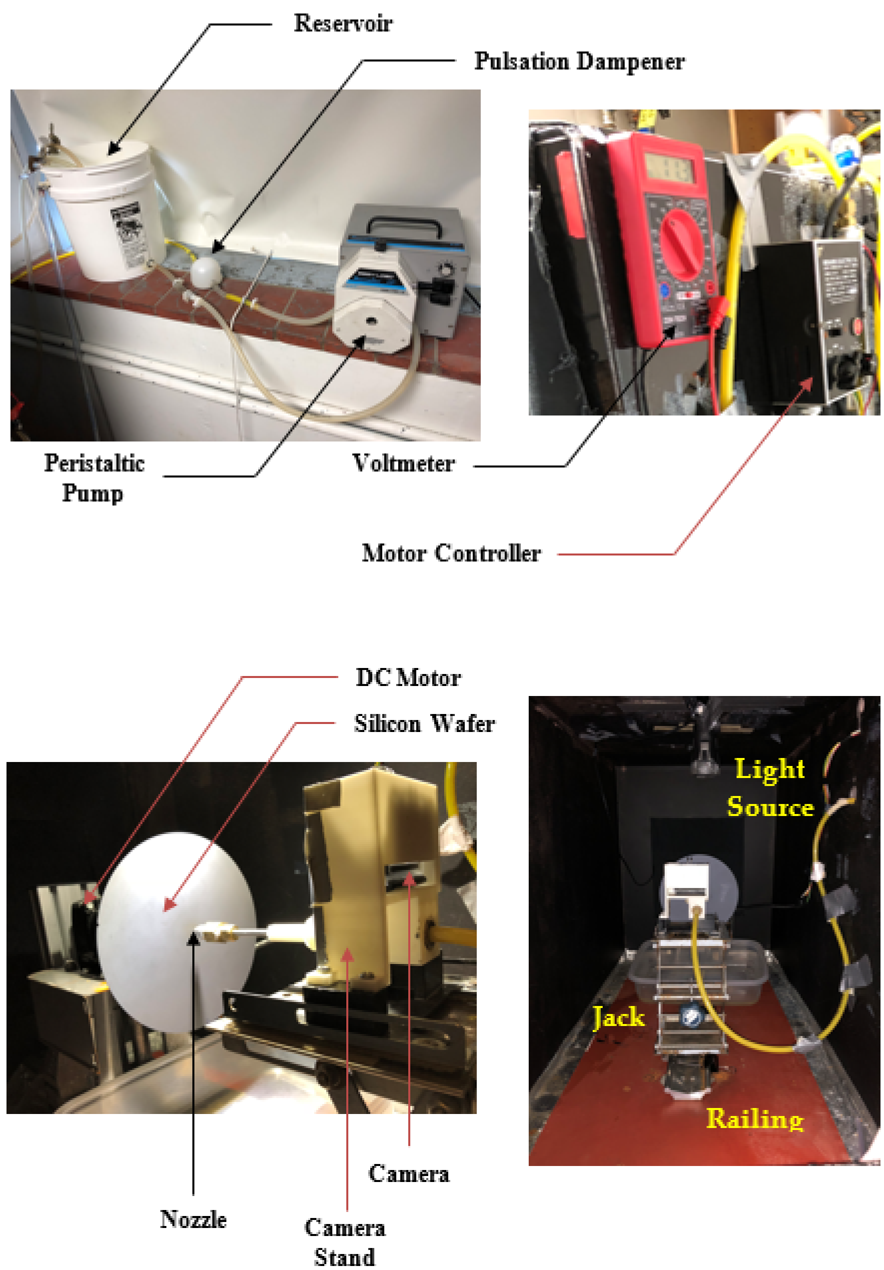

Figure 6: Experimental setup of the system.

4. Results

4.1. Coherent jet analysis

Coherence of the water jet was evaluated based on the onset of capillary instabilities for the cylindrical jets in a horizontal orientation. As shown in Figure 7, a jet goes through various transitions when the jet has to travel longer distances before encountering a surface. The length of a coherent jet (L_c) before the onset of capillary instabilities can be expressed in terms of Weber number (We) determined experimentally as $\frac{L_c}{D_t} \sim 18We^{1/2}$ by Wilson *et al.* (2012) where D_t is the jet diameter.

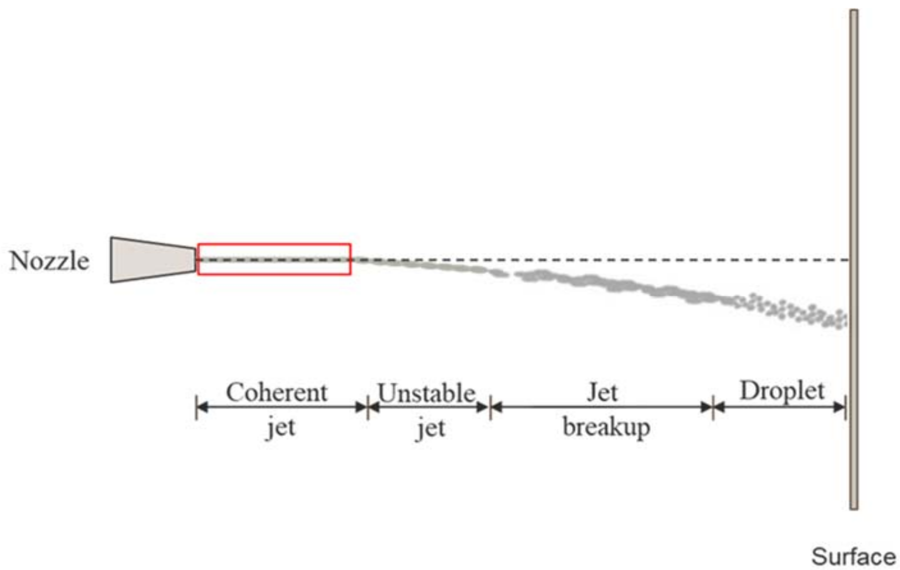

Figure 7: Capillary-driven instability of a water jet under the influence of gravity oriented in a horizontal direction.

Figure 7 indicates Rayleigh-Plateau instability followed by jet breakup and droplet formation when traveling over distances greater than coherent length.

The coherent length for the "worst-case scenario" which is lowest evaluated flow rate (0.1 USGPM or 2.27E-2 m^3/h) for the largest jet diameter (4 mm) was estimated as 588 mm. The jet diameter was considered to be identical to the nozzle diameter as this is a fair assumption for Newtonian water jets that, unlike non-Newtonian fluids, do not undergo extrudate swelling.

4.2. Water jet impingement on vertically oriented non-spinning silicon wafer

Previous experimental work by Wang *et al.* (2013) on hydraulic jump dimensions for glass and PMMA was validated by impinging water jets under similar conditions on a stationary rough silicon wafer. The dimensions were fairly consistent on the existing setup. Comparisons were drawn on hydraulic jump width and height which were determined using a MATLAB® code (Refer appendix B) based on average image analysis over a 10 second video clip recorded at 60 frames per second using a GoPro Hero 4. Multiple trials indicated consistency in hydraulic jump dimensions.

Surface momentum forces act on the surface from impingement point along radial direction till $R^i_\perp$ / $R^i_\parallel$ at which gravitational force balances. Surface tension forces cause protrusion of water out of the flat surface which looks like a corona or a rope of water.

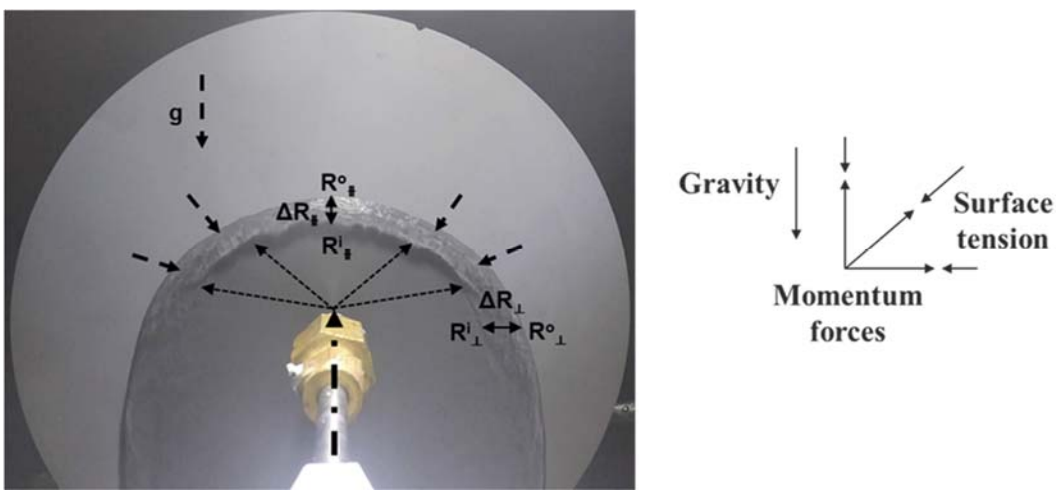

Figure 8: Observed shape of a hydraulic jump on vertical surface with nomenclatures used to quantitatively qualify hydraulic jump.

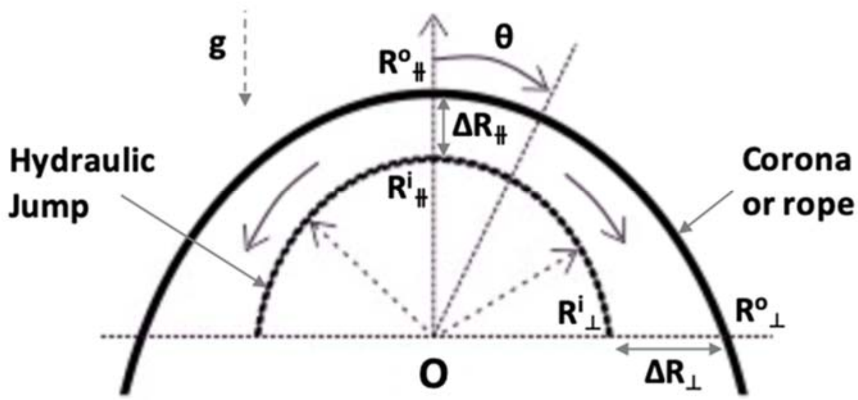

Figure 9: Schematic of hydraulic jump observed during jet impingement on a vertically oriented surface.

The experimental setup was made consistent to the one used by Wang *et al.* (2013) by maintaining the nozzle to wafer distance at 50 mm for stationary hydraulic jump analysis. This exhibited a slack of the coherent jet at lower flowrates for jet diameter of 4 mm.

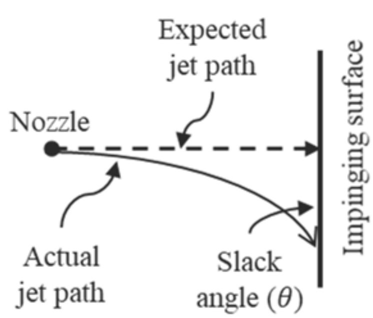

Figure 10: Pictorial representation of slack in the jet path observed low flow rates (< 0.2 USGPM) for 4 m diameter jet.

Non-dimensional hydraulic jump dimensions were plotted against Reynolds number. Hydraulic jump was normalized using jet diameter. Reynolds number was calculated using flowrate through the nozzle.

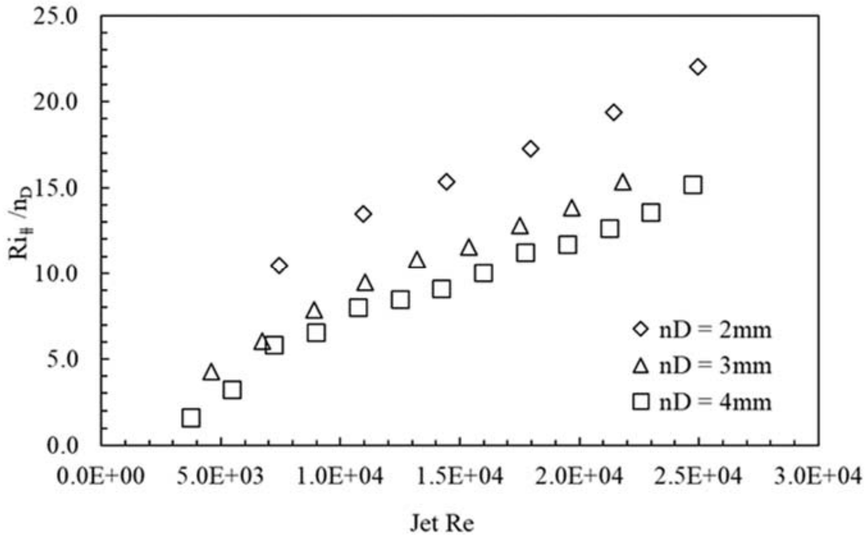

Figure 11: Non-dimensionalized inner height of hydraulic jump (parallel to gravity) plotted against jet Reynolds number exhibits linear trend for varying jet diameter.

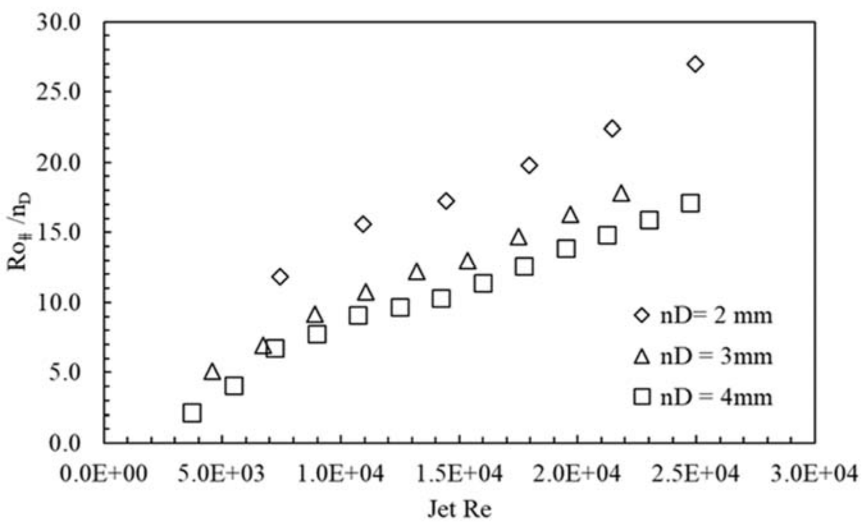

Figure 12: Non-dimensionalized outer height of hydraulic jump (parallel to gravity) plotted against jet Reynolds number exhibits linear trend for varying jet diameter.

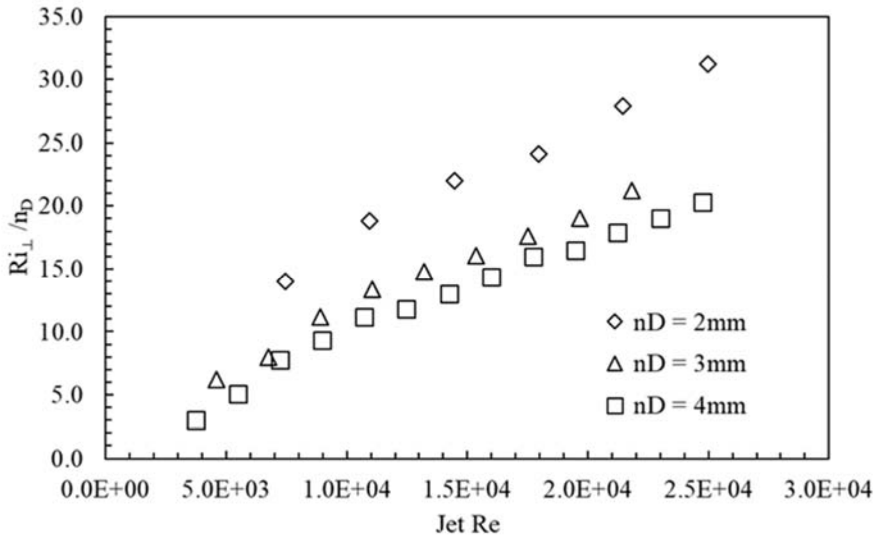

Figure 13: Non-dimensionalized inner width of hydraulic jump (perpendicular to gravity) plotted against jet Reynolds number exhibits linear trend for varying jet diameter.

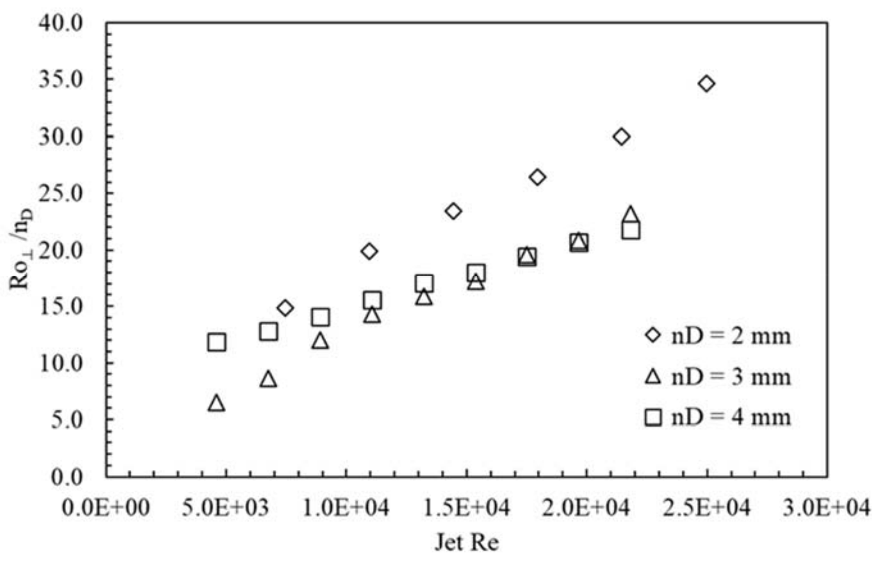

Figure 14: Non-dimensionalized outer width of hydraulic jump (perpendicular to gravity) plotted against jet Reynolds number exhibits linear trend for varying jet diameter.

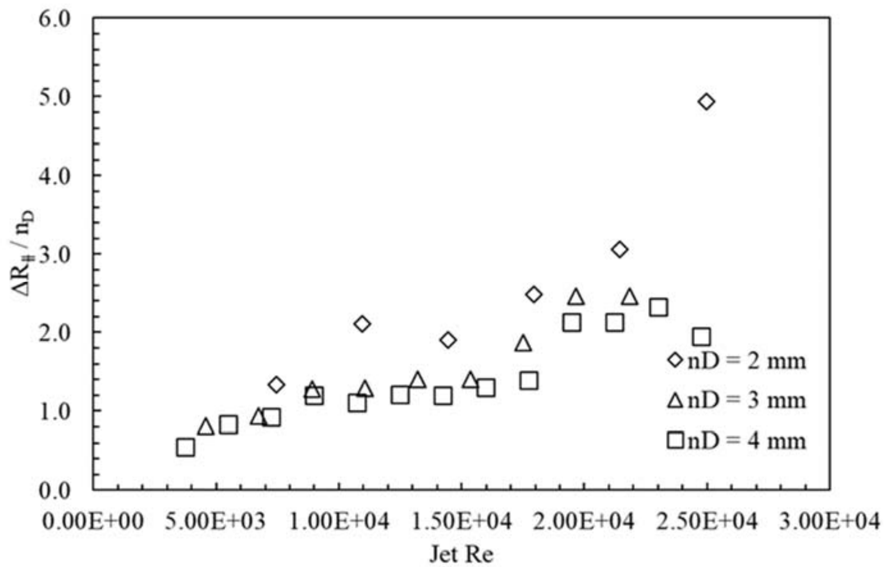

Figure 15: Non-dimensionalized thickness of hydraulic jump (parallel to gravity) plotted against jet Reynolds number.

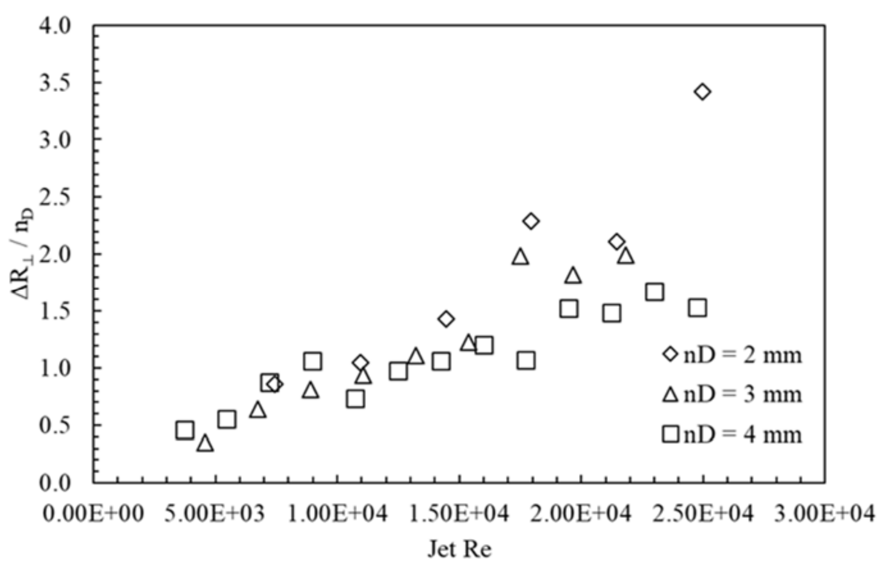

Figure 16: Non-dimensionalized thickness of hydraulic jump (perpendicular to gravity) plotted against jet Reynolds number.

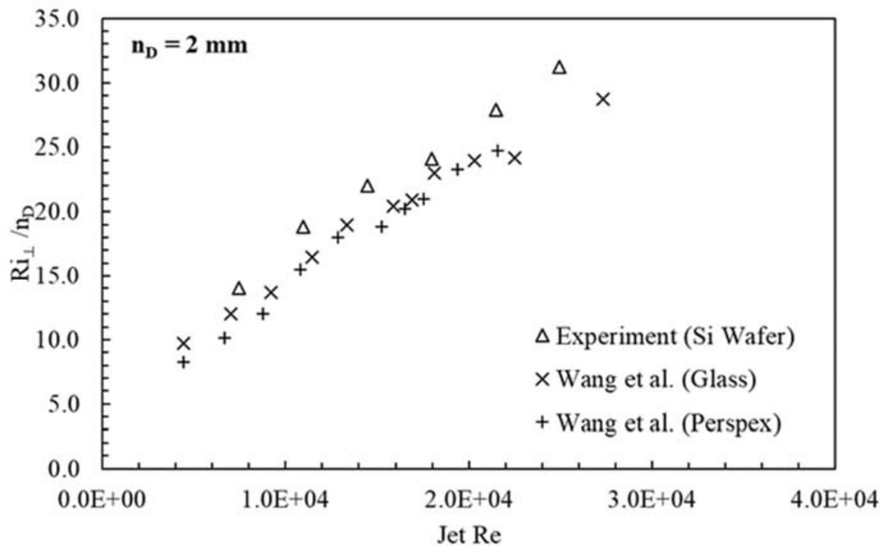

Figure 17: Non-dimensionalized inner width of hydraulic jump (perpendicular to gravity) plotted against jet Reynolds number for a 2 mm nozzle. Trends show a good match with experimental data run by Wang et al. (2013).

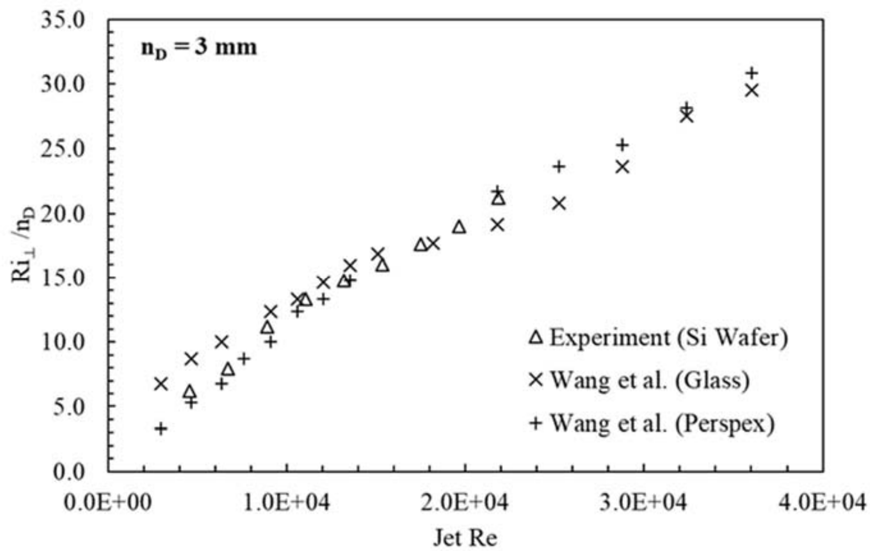

Figure 18: Non-dimensionalized inner width of hydraulic jump (perpendicular to gravity) plotted against jet Reynolds number for a 3 mm nozzle. Trends show a good match with experimental data run by Wang et al. (2013).

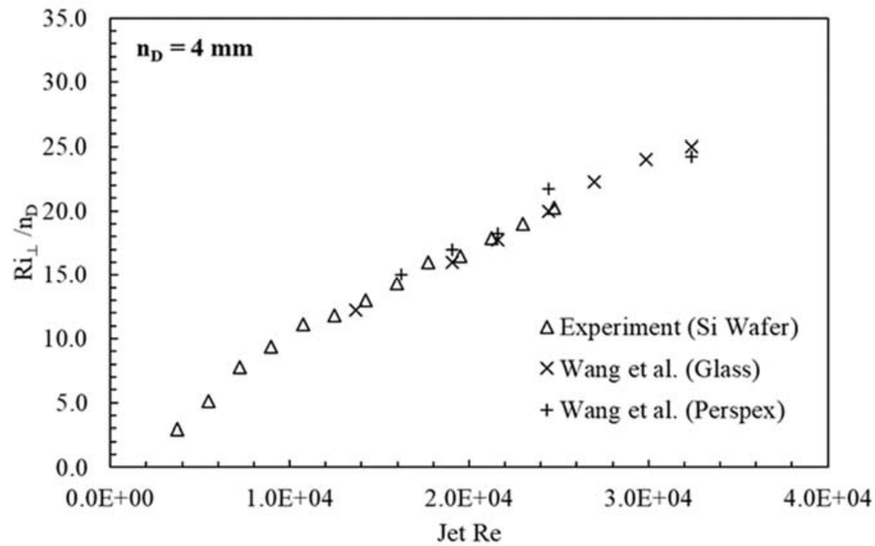

Figure 19: Non-dimensionalized inner width of hydraulic jump (perpendicular to gravity) plotted against jet Reynolds number for a 4 mm nozzle. Trends show a good match with experimental data run by Wang et al. (2013).

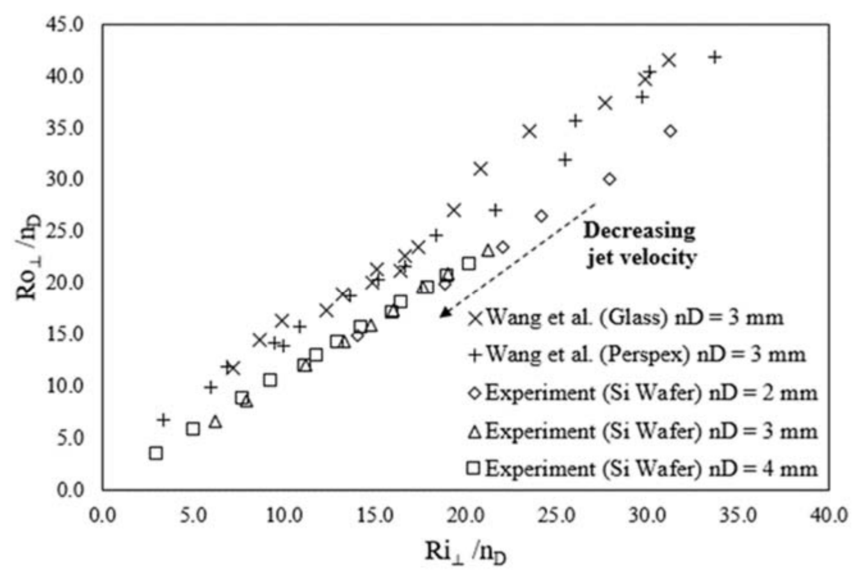

Figure 20: Non-dimensionalized outer width of hydraulic jump (perpendicular to gravity) plotted against non-dimensionalized inner width of hydraulic jump (perpendicular to gravity) superimposed over experimental data by Wang et al. (2013).

The values and trends for hydraulic jump dimensions for the “as-received” 200 mm rough silicon wafer align fairly to Wang *et al.* (2013) data for glass and PMMA (Perspex) surfaces. The height and width of hydraulic jump fails to follow the linear trend at lower jet Reynolds numbers for a 4 mm diameter jet (which is evident in Figures 14 and 19) which can be attributed to the observed slack in the jet causing the impingement to be at an angle less than normal impingement angle referenced from top half of the surface. Figure 11 through 16 indicate that the hydraulic jump dimensions are greater for the 4 mm nozzle when compared to smaller nozzle diameter which can be credited to higher volumetric flowrates resulting in increased rope diameter. Figure 20 shows relationship between the inner and outer width of the hydraulic jump. Wang et al. (2013) expressed a slope value of 1.3 for the glass and Perspex surface but the experimental data on “as-received” 200 mm rough silicon wafer suggests a slope value of 1.1. The shape of hydraulic jump was symmetrical to the point of jet impingement on the surface.

4.3. Water jet impingement on vertically oriented spinning "as-received" silicon wafers

Vertically oriented wafers were spun in clockwise direction using a DC drive with possibility of speed regulation using a motor controller through voltage regulation. A calibration curve (Refer appendix A) was developed relating voltage supply to the rotational speed of wafer. Calibration curves were developed relating rotational speed of wafers to the voltage of the drive. A fluctuation in voltage levels was observed when impinging water jet on the surface but the system was run for long duration of time at a specific rotational speed till the voltage values steadied.

The rotation of surfaces involved introduction of centrifugal force to the previous force balances stated for the stationary hydraulic jump causing the hydraulic jump to undergo transitions, and eventually disappear at the critical rotational speed.

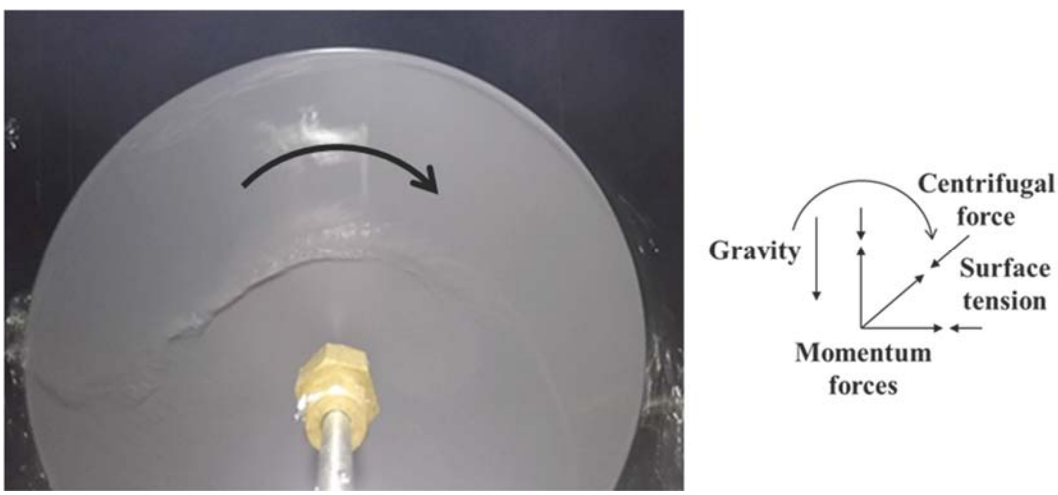

Figure 21: Rotation of "as-received" 200 mm rough silicon wafer in clockwise direction causing change in the shape of the hydraulic jump.

The rotational speed shown in the Figure 21 was 213 RPM which was below the critical rotational speed for jet Reynolds number of 1.58E+04 for a 2 mm diameter water jet. The dynamics of hydraulic jump were observed for horizontal water jets using a 2 mm diameter nozzle. The nozzle to wafer distance was set at 5 mm instead of 50 mm to avoid effect of jet slacking on the hydraulic jump.

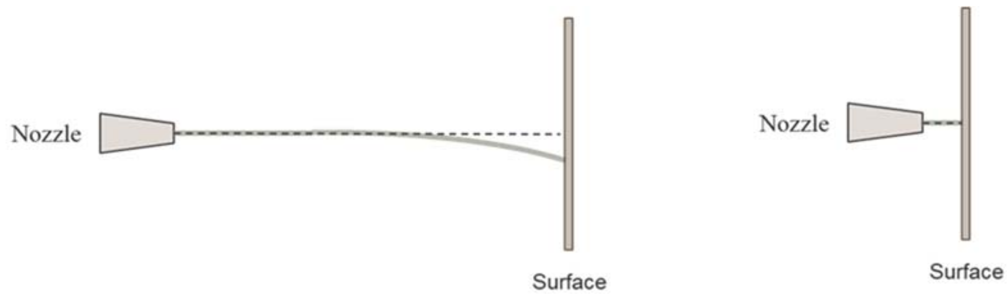

Figure 22: Slacking of jets in the coherent length of the jet under the influence of gravity.

This section covers phenomenological observations of different "as-received" silicon wafers when they were rotated while impinging coherent water jets. Flowrates ranging from 0.1 USGPM to 0.6 USGPM were checked for a nozzle diameter of 2 mm.

4.3.1. Rotation of "as-received" 200 mm rough silicon wafer

"As-received" 200 mm rough silicon wafer (Figure 23) was rotated in clockwise direction at different rotational speeds while being impinged with coherent water jet at different flowrates to understand the changes in hydraulic jump behavior at different rotational speeds.

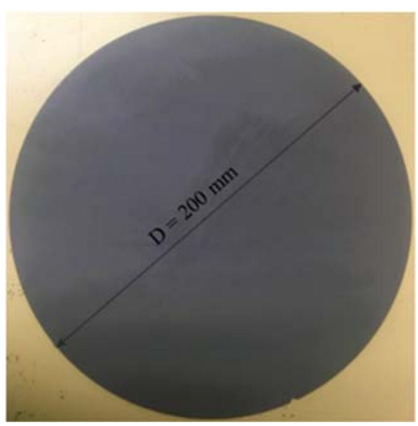

Figure 23: Still image of an "as-received" rough silicon wafer of diameter 200 mm.

At lower rotational speeds, a phenomena (henceforth, referred to as eddies) were observed. Eddies were specifically observed next to the left lip of the hydraulic jump (from the observer's view point) at speeds below 50 rpm. These eddies were observed to be independent of flowrate and appeared at or around similar rotational speeds. The lower rotational speed was limited to 35 rpm for the used motor due to initial torque required to induce smooth rotation of wafer. Figure 24 shows the location of eddies with the video recorder facing the rotating wafer.

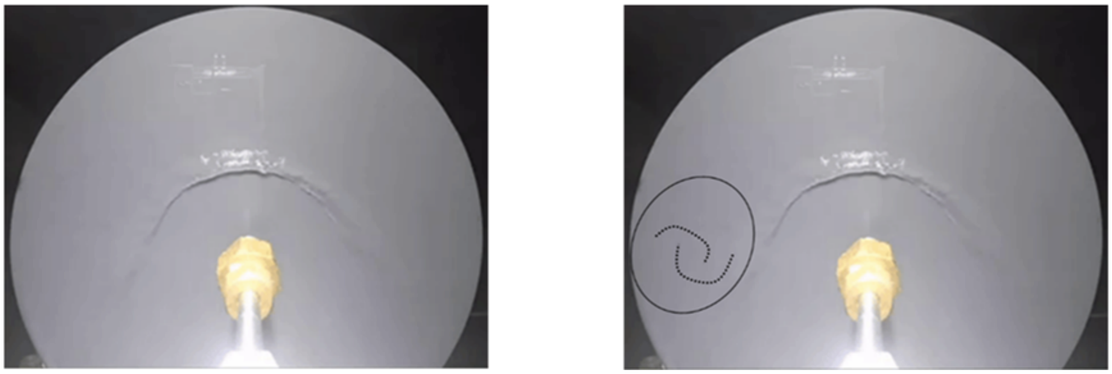

Figure 24: Eddies observed at relatively low rotational speeds (bracketed between 35 RPM and 50 RPM). The still image is at a flowrate of 0.4 USGPM and a rotational speed of 45 RPM.

As the speed of rotation is increased, eddies transition into a phenomenon (henceforth, referred to as secondary hydraulic jump, as seen in Figure 25) that appears next to the hydraulic jump. The secondary hydraulic jump grows with increasing speeds and eventually reaches the edge of the wafer which protrudes along the edge of the wafer.

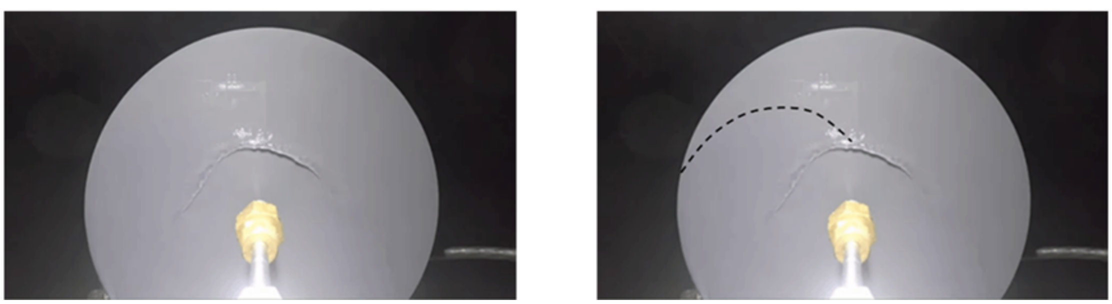

Figure 25: Secondary hydraulic jump observed at relatively rotational speeds over 50 RPM. The still image is at a flowrate of 0.4 USGPM and a rotational speed of 62 RPM.

At higher rotational speeds (unrelated to secondary hydraulic jump, as seen in Figure 26), fringing patterns or ripples were observed at the left lip of the hydraulic jump (from the observer's view point). Such phenomenon was consistently seen till the hydraulic jump disappeared at critical rotational speeds.

Figure 26: Ripples observed at rotational speeds that seemed to be a function of flowrate. The still image is for an "as-received" 200 mm rough wafer at a flowrate of 0.4 USGPM and a rotational speed of 121 RPM.

The image matrices in Figure 27 and 28 summarize various transitions captured at different rotational speed of the wafer. All of these transitions were observed for flow rates used in this experiment. Figure 28 shows disappearance of hydraulic jump at specified rotational rate. The timescale for the hydraulic jump disappearance was observed to be less than 5 seconds.

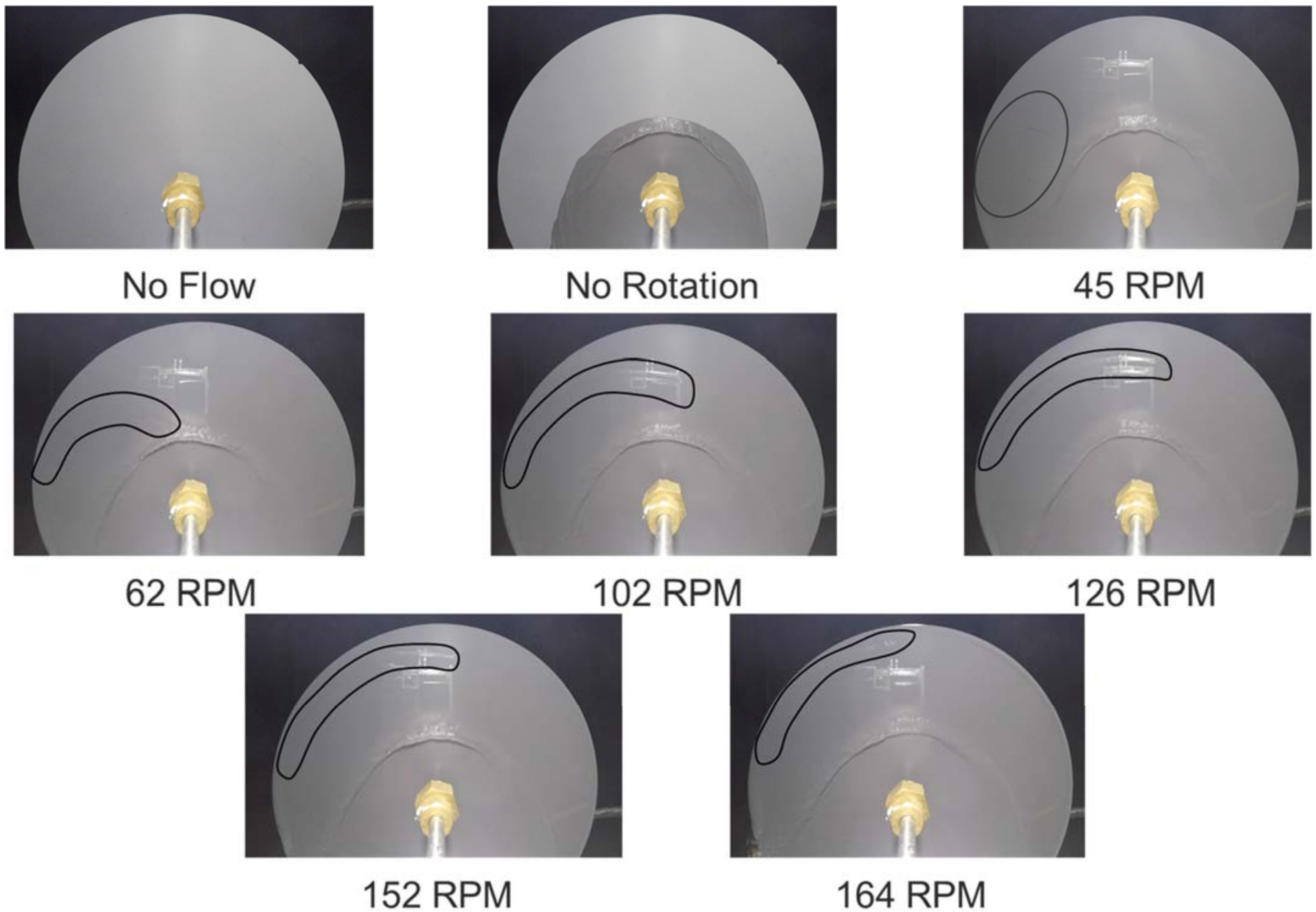

Figure 27: Image matrix (part-1) for an "as-received" 200 mm rough silicon wafer at different rotational speeds when impinging coherent water jet at a flowrate of 0.4 USGPM.

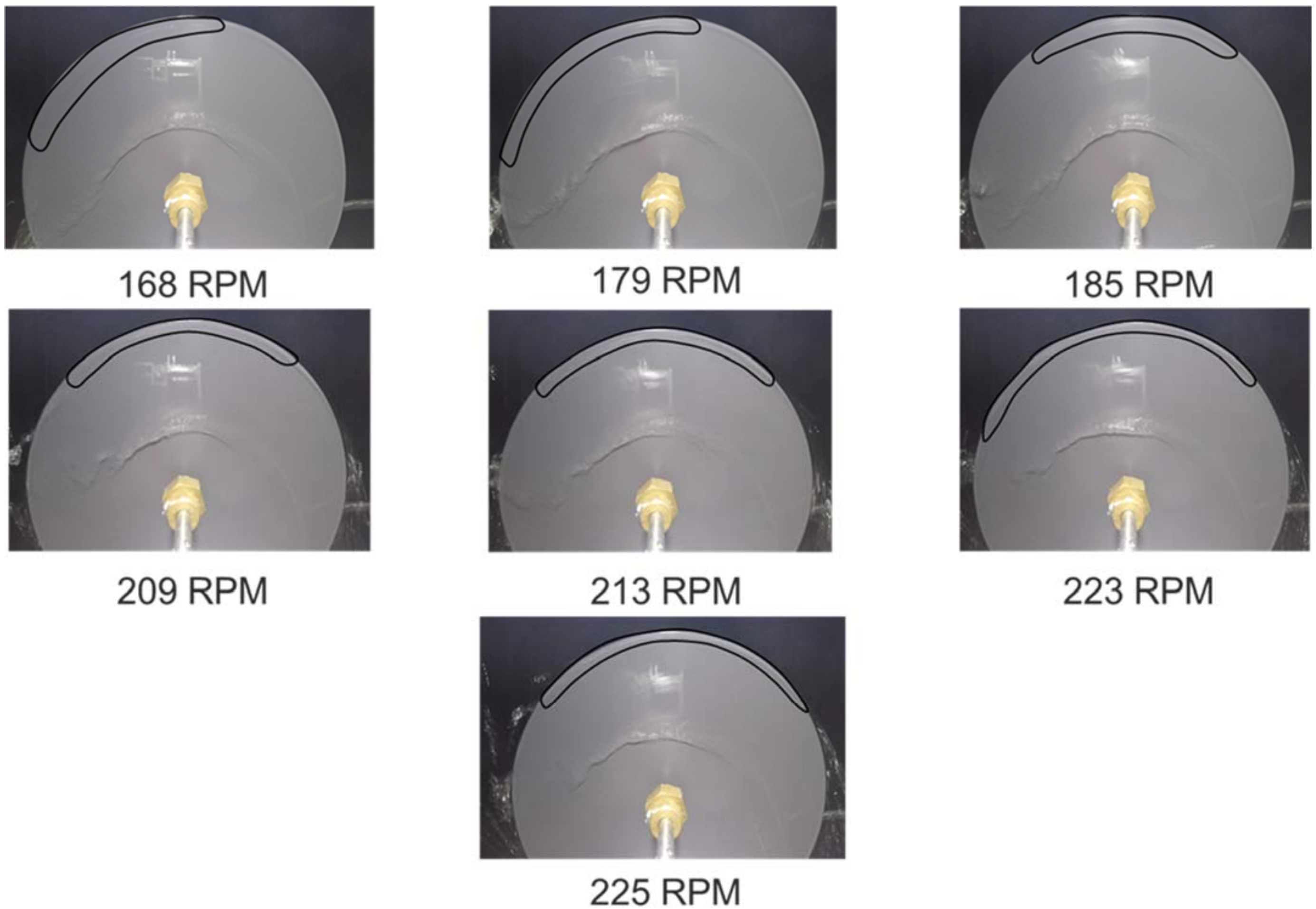

Figure 28: Image matrix (part-2) for an "as-received" 200 mm rough silicon wafer at different rotational speeds when impinging coherent water jet at a flowrate of 0.4 USGPM.

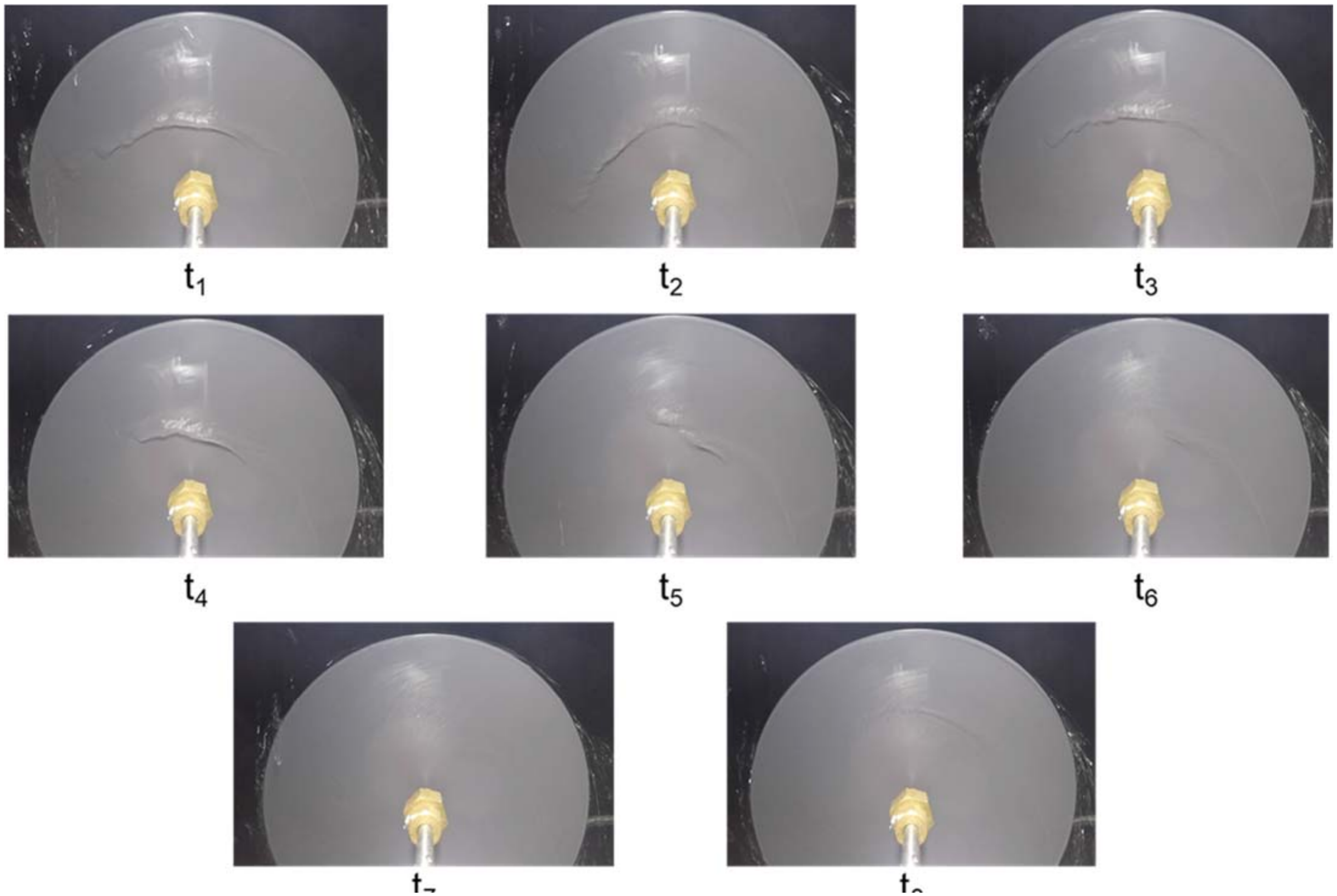

Figure 29: Disappearance of hydraulic jump for an "as-received" 200 mm rough silicon wafer at 243 RPM when impinging coherent water jet at a flowrate of 0.4 USGPM. The time-scale ($t_1 \rightarrow t_8$) at critical rotational speed for disappearance of hydraulic jump is bracketed between 3 – 5 seconds.

4.3.2. Rotation of "as-received" 165 mm smooth silicon wafer

An "as-received" 165 mm smooth silicon wafer (Figure 30) having a mirror finish was rotated in clockwise direction at different rotational speeds while being impinged with a coherent water jet at different flowrates to understand the changes in hydraulic jump behavior at different rotational speeds.

Figure 30: Still image of an "as-received" smooth silicon wafer of diameter 165 mm.

The wafer exhibited slip-stick phenomena when rotated at different speeds. At low rotational speeds, the water tended to stick to the surface as shown in Figure 31. The still image was captured at a wafer rotational speed of 76 RPM with coherent water jet flowrate of 0.4 USGPM. As the speed of rotation was increased, the generated centrifugal force aided in slipping the water molecules on the surface (Figure 32) of this wafer unlike the 200 mm rough wafer where the water tended to easily wet the surface. No secondary hydraulic jump was observed on the "as-received" 165 mm smooth silicon wafer.

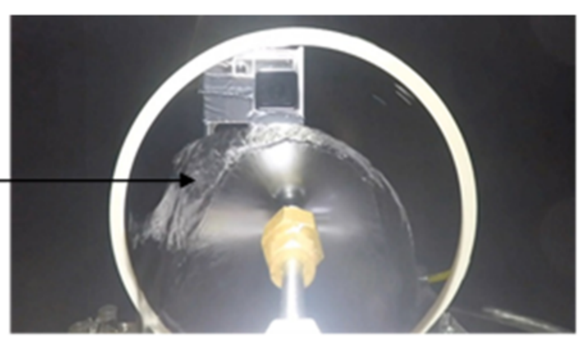

Figure 31: Sticking phenomena on an "as-received" 165 mm smooth silicon wafer.

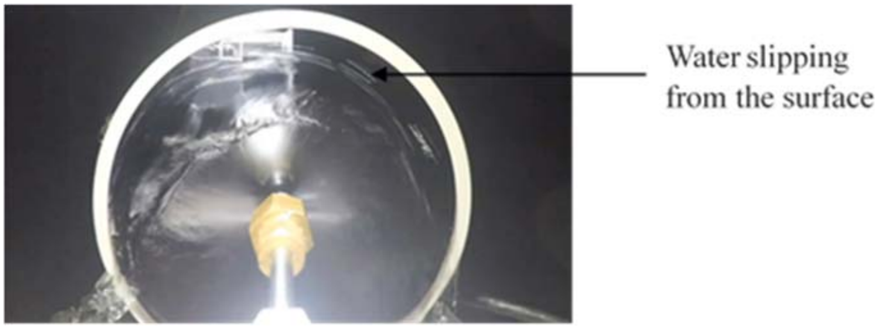

Figure 32: Slipping phenomena on an "as-received" 165 mm smooth silicon wafer.

Ripples were observed at higher wafer rotational speeds which can be related to the flowrate of the impinging jet. The ripples seemed to exist on the surface of the wafer even after the disappearance of hydraulic jump.

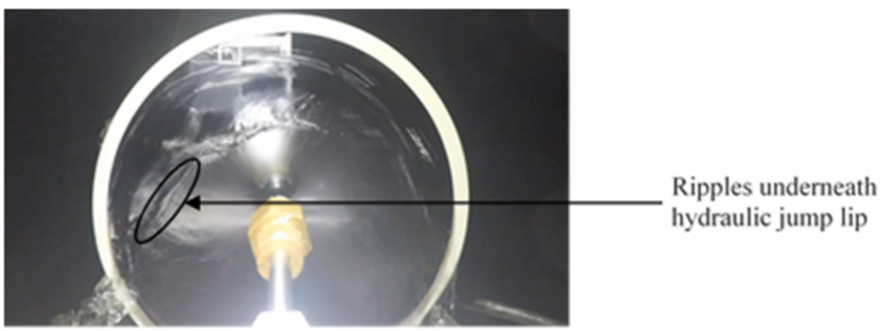

Figure 33: Ripples observed at rotational speeds that seemed to be a function of flowrate. The still image is for an "as-received" 165 mm smooth silicon wafer at a flowrate of 0.4 USGPM and a rotational speed of 131 RPM.

The image matrices in Figures 34 and 35 summarize various transitions captured at different rotational speed of the wafer. All of these transitions were observed for flow rates used in this experiment. Figure 35 also covers different hydraulic jump transitions at critical rotational speed leading to hydraulic jump disappearance.

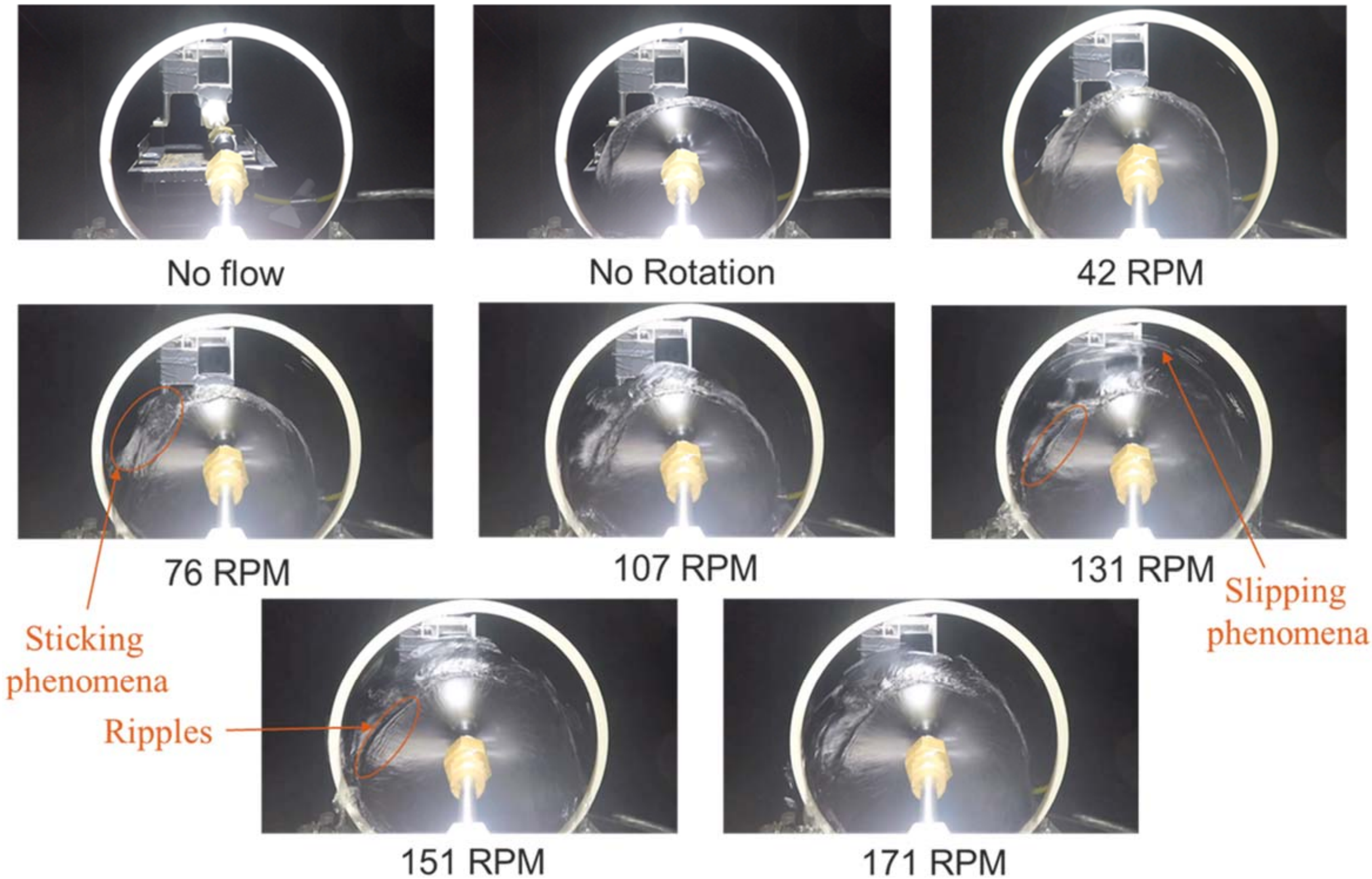

Figure 34: Image matrix for an "as-received" 165 mm smooth silicon wafer at different rotational speeds when impinging coherent water jet at a flowrate of 0.4 USGPM.

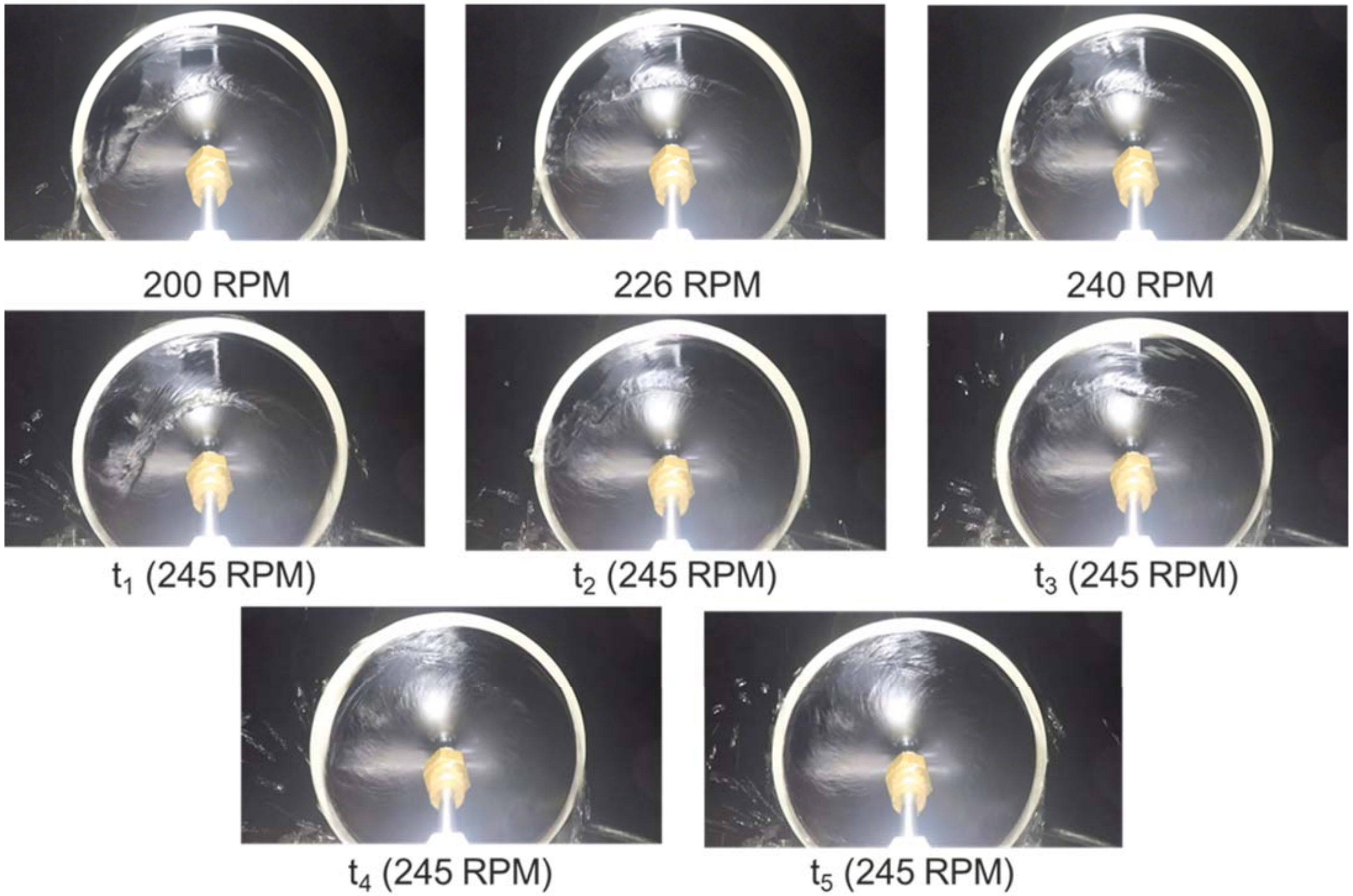

Figure 35: Image matrix for an "as-received" 165 mm smooth silicon wafer at different rotational speeds when impinging coherent water jet at a flowrate of 0.4 USGPM. Disappearance of hydraulic jump was captured at 245 RPM. . The time-scale ($t_1 \rightarrow t_5$) at critical rotational speed for disappearance of hydraulic jump is bracketed between 3 - 5 seconds.

4.3.3. Rotation of "as-received" 300 mm smooth silicon wafer

An "as-received" 300 mm smooth silicon wafer (Figure 36) having a mirror finish was rotated in clockwise direction at different rotational speeds while being impinged with a coherent water jet at different flowrates to understand the changes in hydraulic jump behavior at different rotational speeds.

Figure 36: Still image of an "as-received" smooth silicon wafer of diameter 165 mm.

At lower rotational speeds, eddies were observed. Eddies were specifically observed next to the left lip of the hydraulic jump (from the observer's view point) at speeds below 40 rpm (Figure 37). These eddies were observed to be independent of flowrate and appeared at or around similar rotational speeds.

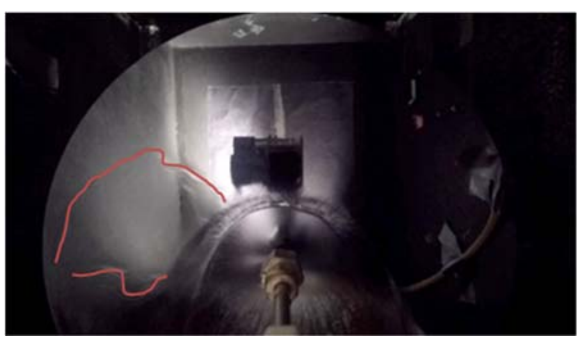

Figure 37: Eddies observed at low rotational speeds. The still image is at a flowrate of 0.4 USGPM and a rotational speed of 30 RPM.

As the speed of rotation is increased, eddies transition into a phenomenon (heretofore, referred to as secondary hydraulic jump) that appears next to the hydraulic jump (Figure

38). The secondary hydraulic jump grows with increasing speeds and eventually reaches the edge of the wafer which protrudes along the edge of the wafer.

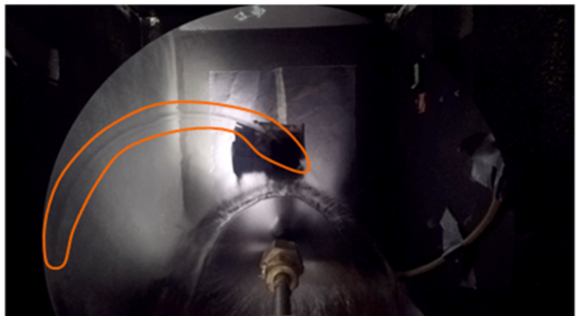

Figure 38: Eddies transition into a secondary hydraulic jump. The still image is at a flowrate of 0.4 USGPM and a rotational speed of 44 RPM.

At higher rotational speeds (unrelated to secondary hydraulic jump), fringing patterns or ripples (Figure 39) were observed unrelated to the secondary hydraulic jump at the left lip of the hydraulic jump (from the observer's view point). The phenomenon was consistently seen till the hydraulic jump disappeared at critical rotational speeds.

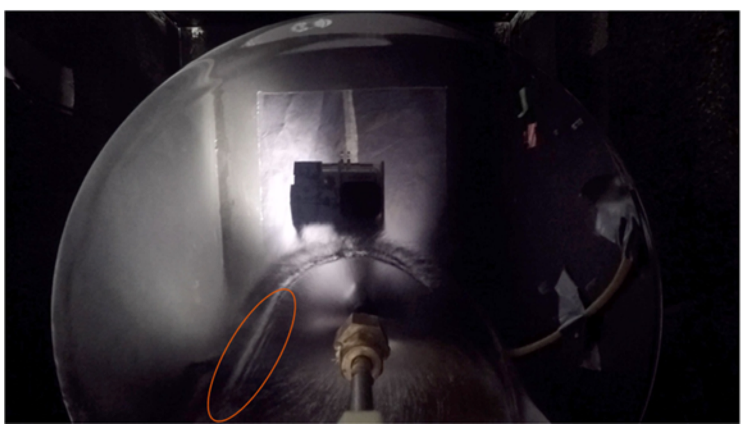

Figure 39: Ripples observed at rotational speeds that seemed to be a function of flowrate. The still image is for an as-received 300 mm smooth wafer at a flowrate of 0.4 USGPM and a rotational speed of 110 RPM.

The image matrices in Figures 40 and 41 summarize various transitions captured at different rotational speeds of the wafer. All of these transitions were observed for flow rates used in this experiment. Figure 42 shows disappearance of hydraulic jump at specified rotational rate. The timescale for the hydraulic jump disappearance was observed to be less than 5 seconds.

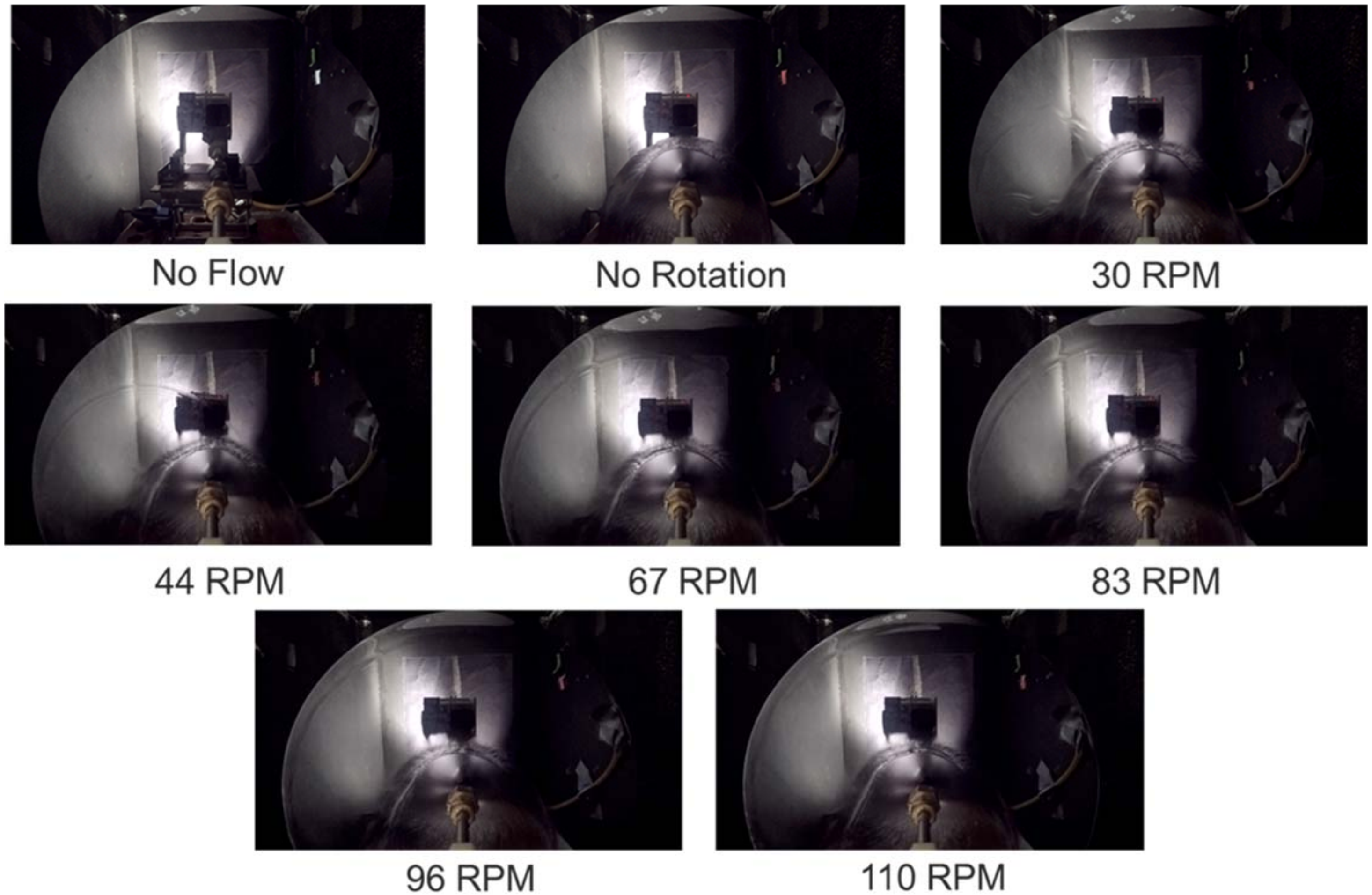

Figure 40: Image matrix (part-1) for an "as-received" 300 mm smooth silicon wafer at different rotational speeds when impinging coherent water jet is at a flowrate of 0.4 USGPM.

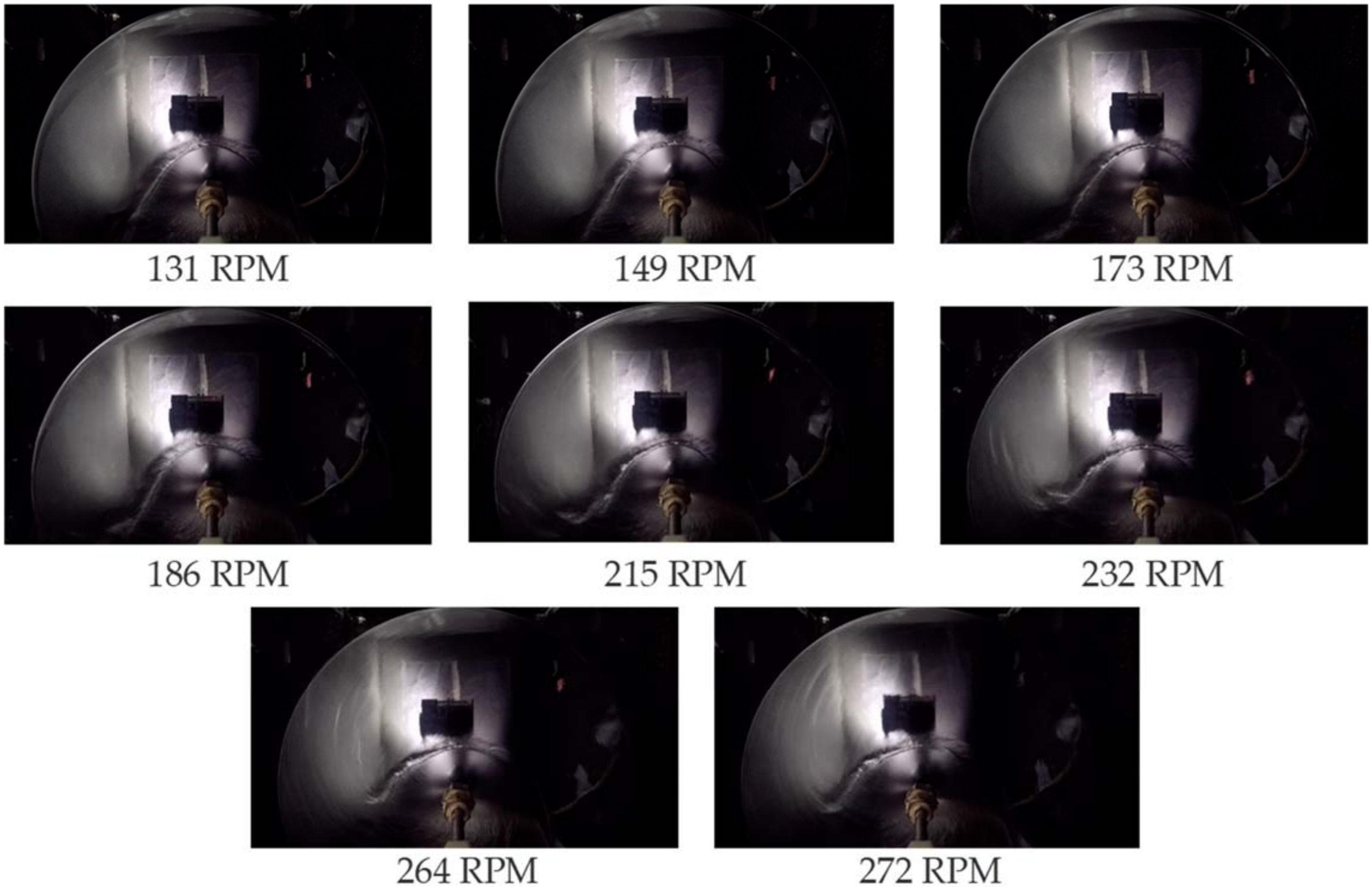

Figure 41: Image matrix (part-2) for an "as-received" 300 mm smooth silicon wafer at different rotational speeds when impinging coherent water jet is at a flowrate of 0.4 USGPM.

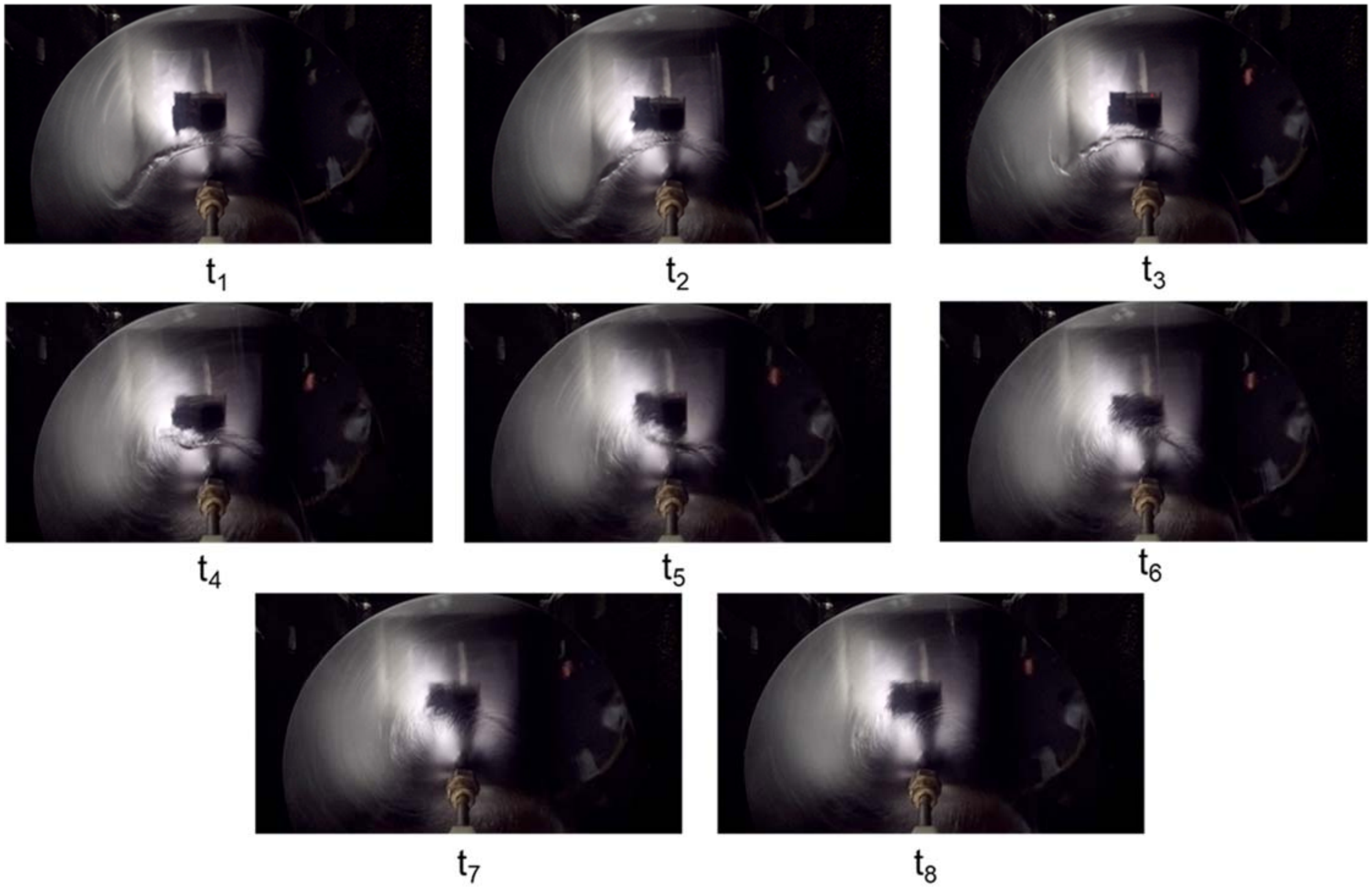

Figure 42: Disappearance of hydraulic jump for an "as-received" 300 mm smooth silicon wafer at 272 RPM when impinging coherent water jet is at a flowrate of 0.4 USGPM. The time-scale ($t_1 \rightarrow t_8$) at critical rotational speed for disappearance of hydraulic jump is bracketed between 3 - 5 seconds.

4.4. Surface characterization by contact angle

Contact angle measurements were used to characterize the different surfaces used in these studies. Contact angle is a reliable technique to understand the fluid interactions on a surface. This technique can be a good indicator of the wetting characteristics of the surface under study and can provide qualitative indication of surface topography.

Figure 43 shows different interactions that a fluid can have on a solid surface depending on the type of fluid and (or) the surface. Contact angle can be defined as the angle formed by the intersection of the liquid-solid interface and the liquid-vapor interface (in this case, ϴ). The interface where all three phases co-exist is called the "three-phase contact line".

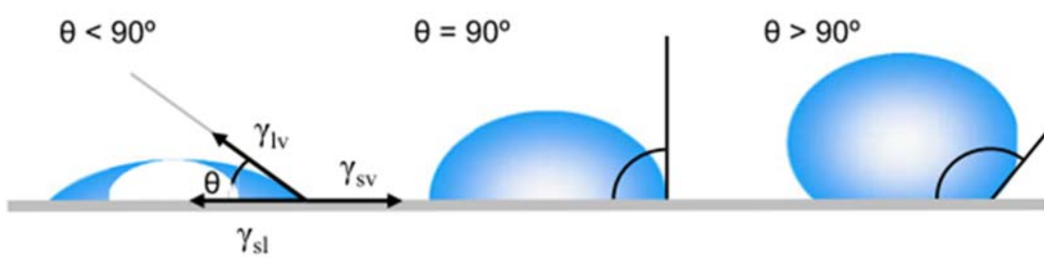

Figure 43: Illustration of different behaviors that a liquid drop can exhibit on a solid surface.

The figure above distinctly indicates that lower contact angles relate to spreading of the liquid on the solid surface (wetting). Thus, the shape of the droplet is directed by the surface tension of the fluid. In this study, high purity water was used for all measurements. The contact angle reflects both, the interaction of the fluid with the surface (surface energy) and the roughness of the surface. For example, water on a smooth silicon wafer will have a higher contact angle than water on a silicon wafer with higher degree of roughness.

The contact angle of a liquid drop on a solid surface can be analyzed using mechanical equilibrium of the drop under three interfacial tensions (as indicated in Figure 43).

$$\gamma_{lv} cos\theta = \gamma_{sv} - \gamma_{sl}$$

where γ_{lv}, γ_{sv} and γ_{sl} represent the liquid-vapor, solid-vapor, and solid-liquid interfacial tensions, respectively, and θ is the contact angle. This angle is a representation of static state of the droplet. However, in reality, there exist metastable states if a droplet on the solid surface which can be better understood by evaluating "dynamic" contact angle which involves actual motion of three-phase contact line. The contact angles formed by expanding and contracting the liquid are referred to as the advancing and receding contact angles, respectively. Along the surface, the advancing contact angle typically tends towards a maximum value while the receding contact angle tends towards a minimum value with the difference representing contact angle hysteresis. Such a hysteresis is a true representation of fluid interaction on surface. These techniques were not used in these studies but may be useful for future work on surface roughness effects on wettability.

Static contact angle tests along the radii of the "as-received" smooth (165 mm) and rough (200 mm) wafers were performed to understand the behavior of surfaces with and without surface roughness. First Ten Angstroms goniometer (Model FTA-135) were used in these studies. Droplet volumes of 5 μL and 10 μL were used on both the surfaces to understand the effects of surface roughness and droplet volume on contact angle. 3 trials at 'n' locations were performed on rough and smooth surfaces and the results are summarized in Table 1, an average standard deviation of ±11.6° was observed for the 200 mm rough silicon surface as against an average standard deviation of ±1.9° for the 165 mm smooth silicon wafer.

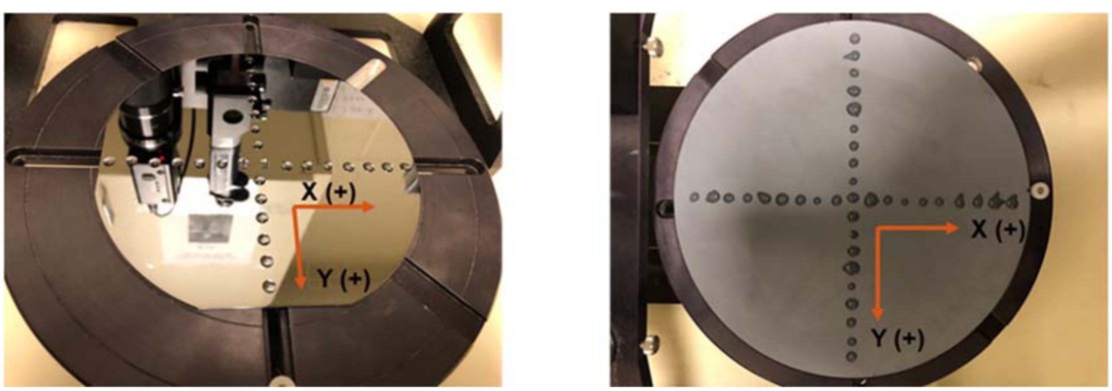

Figure 44: Wafer alignment on FTA-135 stand for measuring contact angle along marked diameter of the wafer along X and Y directions in a Cartesian coordinate system.

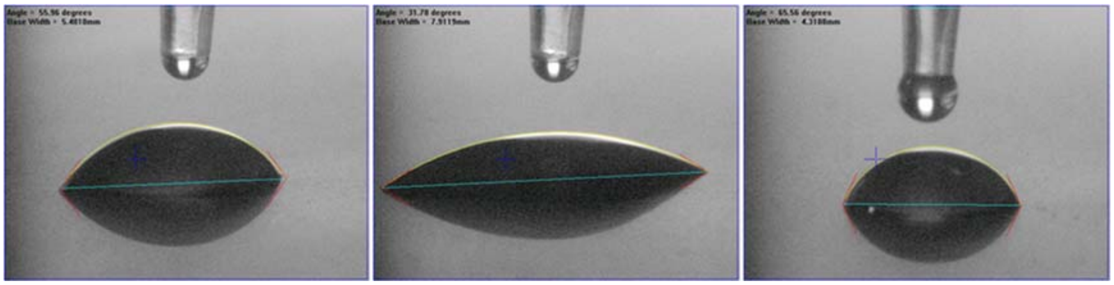

Figure 45: Three contact angle trials on rough Si wafer at Y +60 mm spot dropping 5 µL water droplet.

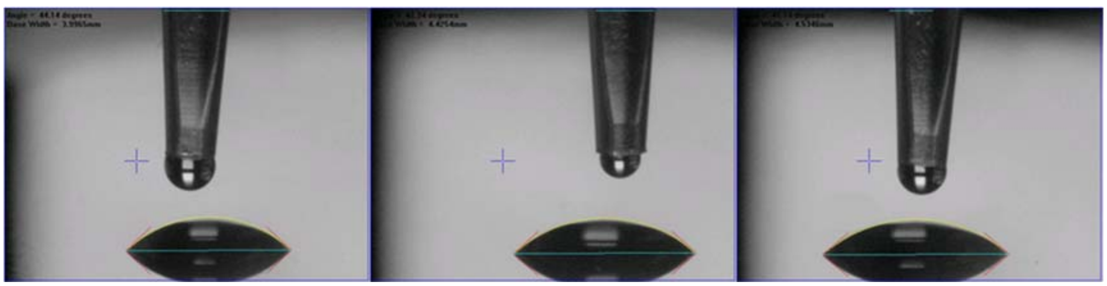

Figure 46: Three contact angle trials on smooth Si wafer at Y +60 mm spot dropping 5 µL water droplet.

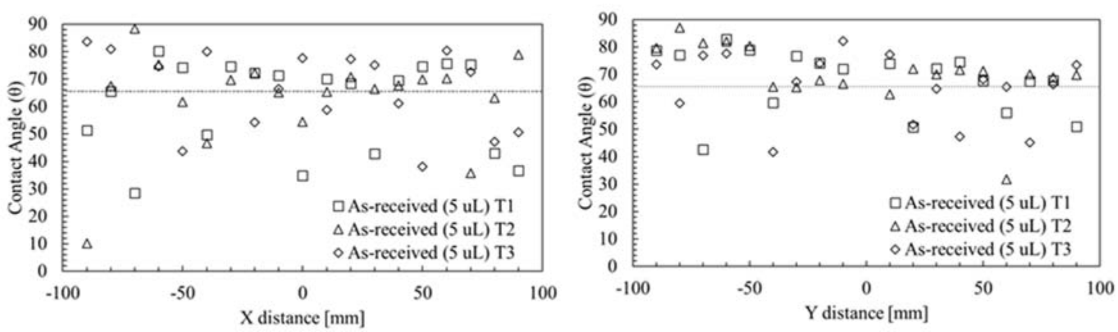

Figure 47: Contact angle measurements as a function of radius of rough Si wafer surface (Wafer diameter = 200 mm). Water droplet size of 5 µL was used. Dotted horizontal line shows mean contact angle for all of the measured data which was estimated to be 65.5º ± 11.6º.

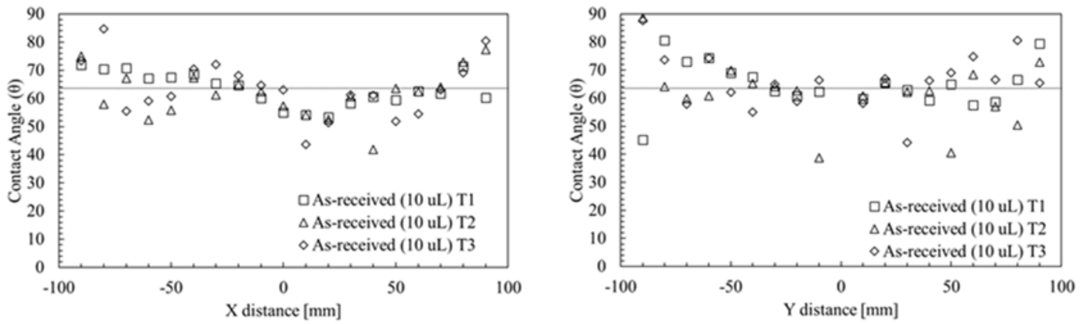

Figure 48: Contact angle measurements as a function of radius of rough Si wafer surface (Wafer diameter = 200 mm). Water droplet size of 10 µL was used. Dotted horizontal line shows mean contact angle for all of the measured data which was estimated to be 63.6º ± 6.5º.

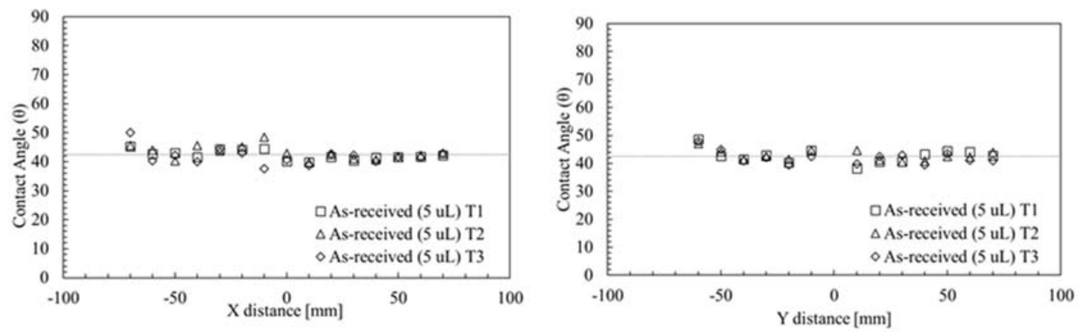

Figure 49: Contact angle measurements as a function of radius of smooth Si wafer surface (Wafer diameter = 165 mm). Water droplet size of 5 µL was used. Dotted horizontal line shows mean contact angle for all of the measured data which was estimated to be 42.5º ± 1.3º.

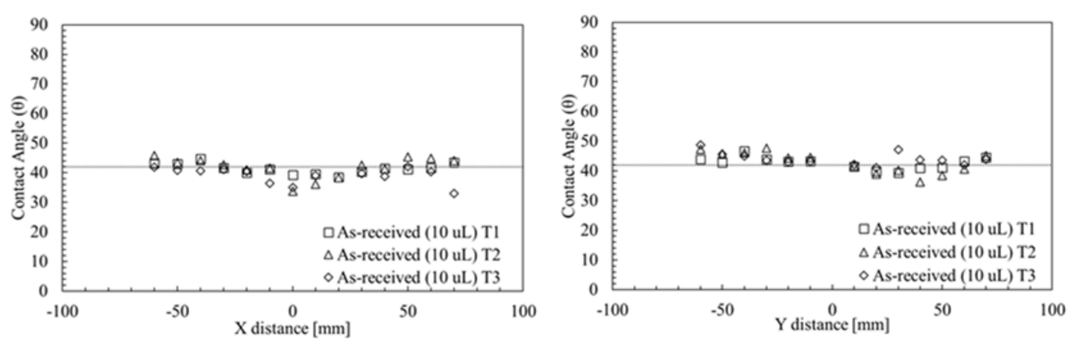

Figure 50: Contact angle measurements as a function of radius of smooth Si wafer surface (Wafer diameter = 165 mm). Water droplet size of 10 µL was used. Dotted horizontal line shows mean contact angle for all of the measured data which was estimated to be 42º ± 1.9º.

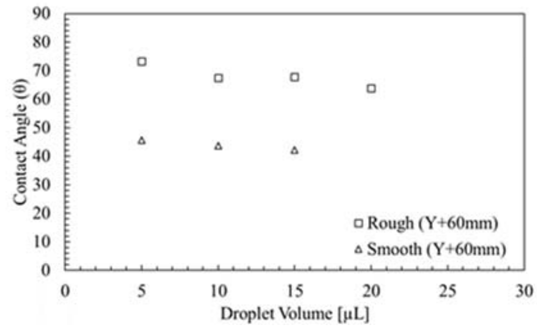

Figure 51: Contact angle measurements as a function of increasing droplet volume on rough and smooth Si wafer surfaces.

Figure 51 shows change in contact angle values with increasing droplet volume on both, rough and smooth "as-received" surfaces. Both the surfaces show drop in contact angle with increasing droplet volume resulting due to the weight of the water droplet.

The contact angle measurements were performed for a 300 mm diameter smooth silicon wafer which exhibited a mean contact angle of 57.6° with an average standard deviation of ±1.9°.

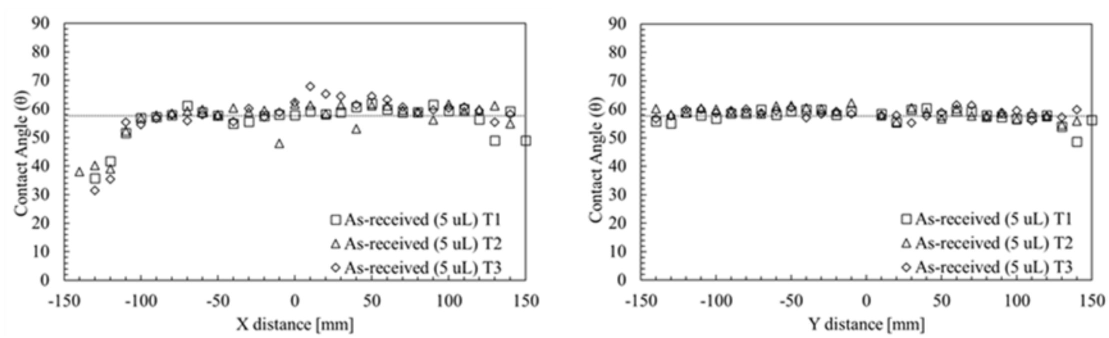

Figure 52: Contact angle measurements as a function of radius of smooth Si wafer surface (Wafer diameter = 300 mm). Water droplet size of 10 µL was used. Dotted horizontal line shows mean contact angle for all of the measured data which was estimated to be 57.6º ± 1.9º.

Table 1: Average contact angle values for "as-received" silicon wafers used in the experiment.

Wafer type and dia.		Droplet Volume [μL]	Avg. Contact Angle [°]	Avg. Std. Dev. [°]	Figure
As-received smooth	165	5	42.5	1.3	49
		10	42.0	1.9	50
	300	5	57.6	1.9	52
As-received rough	200	5	65.5	11.6	47
		10	63.6	6.5	48

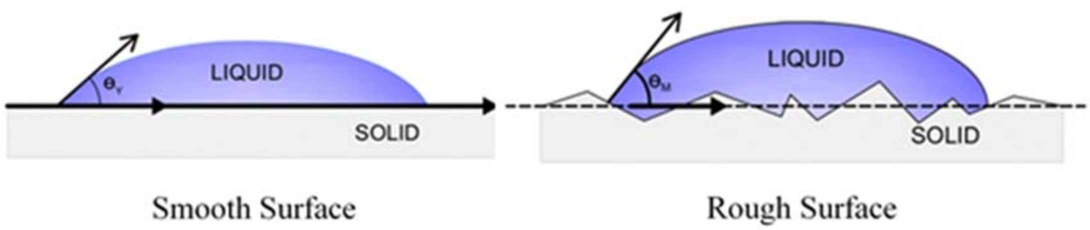

Figure 53: Illustration of contact angles for an even and a rough surface.

Results show that the contact angle tests for the "as-received" rough silicon wafer are not repeatable due to troughs and crevices on the surface that end up pinning the water droplet leading to higher contact angles. The surface roughness is also indicated by the inflated standard deviation in contact angle observed for the rough surface. For the "as-received" smooth wafer, a low value of standard deviation is indicative of less surface variability which is interpreted as surface roughness. The mechanistic behavior of the droplet on both these surfaces types can be summarized in Figure 53. The contact angle for the smooth surface (θ_Y) is lower than the contact angle for the rough surface (θ_M).

As indicated, due to pinning of droplet on a rough surface, contact angles values can be inflated and may not necessarily be the indication of surface wettability (surface energy) but dictated by the surface topography.

4.5. Radio Corporation of America (RCA) Cleaning Process

The RCA wash developed by Werner Kern at RCA laboratories in 1965 is for removing organic and ionic contaminants from silicon wafer surfaces. There are various adaptations of this method but, in this study, the two-step process described below was used. The first part of this process focusses on oxidative desorption and complexing of organic residue with H_2O_2-NH_4OH-H_2O. 65 mL 27% NH_4OH was added to 325 mL DI water in a Pyrex® beaker and heated to 70±5°C. The beaker was removed from the hot plate and 65 mL 30% H_2O_2 was added which results in vigorous bubbling. The 165 mm diameter smooth silicon wafer was soaked in this solution for 15 minutes (during which the bubble generation eventually stopped). The wafer was then removed and washed in a bath under flowing DI water. Once the pH of the water used for wash was close to neutral (~7), the wafer was left submerged in DI water until the materials were ready for the second part of the wash.

Figure 54: Step 1 of the RCA wash for the 165 mm smooth wafer indicates the onset of removal of organic contaminants indicated by the intensity of bubble generation which eventually subdues over a span of 15 minutes.

This process leaves a thin layer of oxide on the surface which can be cleaned by HF wash. However, this step was not employed as the oxide layer regrows immediately after rinsing the surface post HF wash. The final process removes ionic contaminants from the surface using mixture H_2O_2-HCl-H_2O. 50 mL 27% HCl was added to 300 mL DI water in a Pyrex® beaker and heated to 70±5°C. The beaker was removed from the hot plate and 50 mL 30% H_2O_2 was added which results in vigorous bubbling. The "as-received" 165 mm smooth silicon wafer was soaked in this solution for 15 minutes (during which the bubble generation eventually stopped). The wafer was then removed and washed under flowing DI water. Once the pH of the water used for wash was close to neutral (~7), the wafer was left submerged in DI water. With the notion that the surface behavior will change if exposed to air over long duration of time, the wafer was submerged in water till contact angle tests and the experiments were run. The surface was dried with nitrogen gas whenever the surface was either part of an experiment or characterized. The contact angle characterization technique showed that the contact angle value dropped significantly for the cleaned surfaces (Table 2).

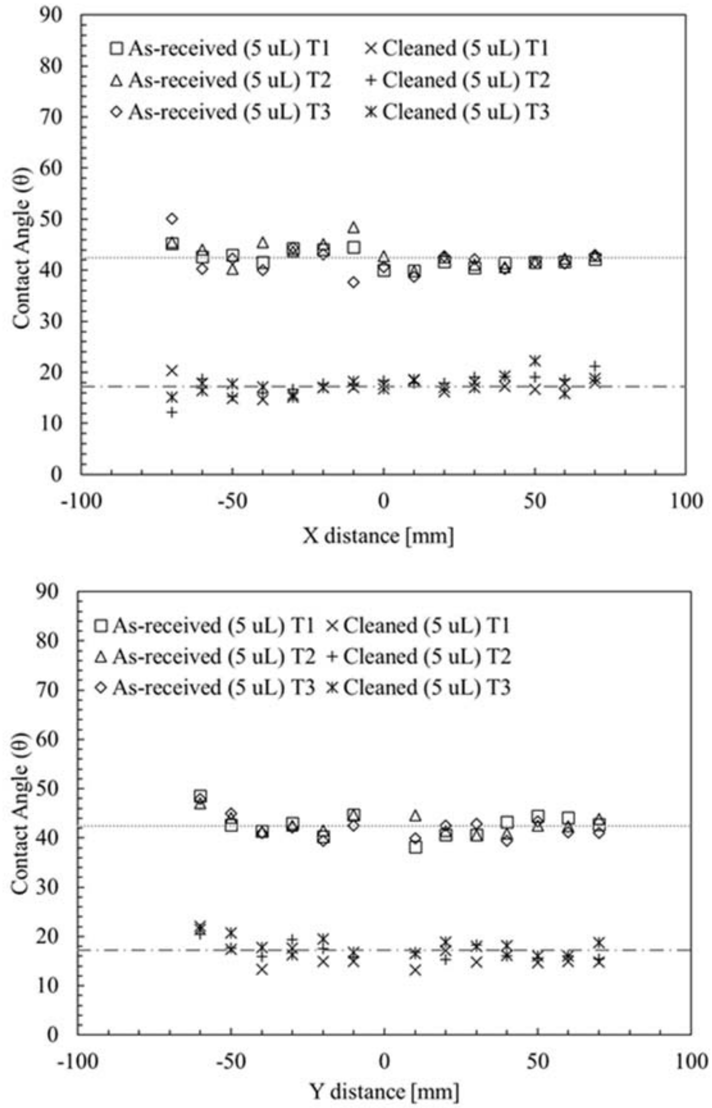

Figure 55: Contact angle of the cleaned 165 mm smooth silicon wafer compared to the as-received smooth silicon wafer.

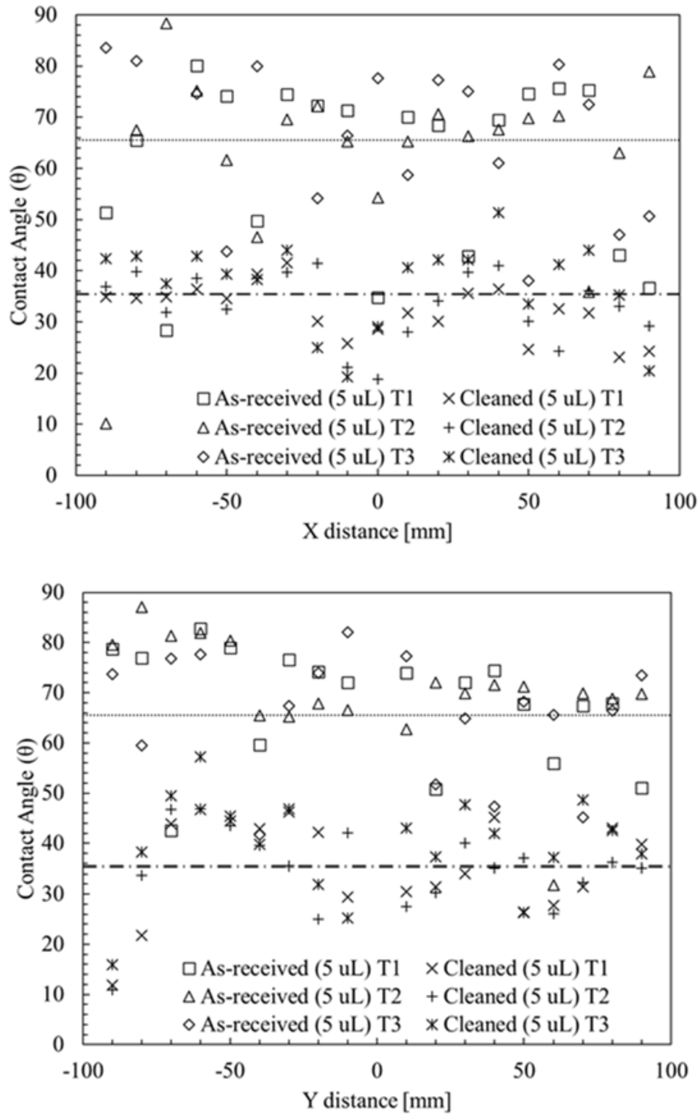

Figure 56: Contact angle of the cleaned 200 mm rough silicon wafer with respect to the as-received rough silicon wafer.

Table 2: Average contact angle values for "as-received" and cleaned silicon wafers.

Wafer type and dia.		Droplet Volume [µL]	Avg. Contact Angle [°]	Avg. Std. Dev. [°]	Figures
As-received smooth	165	5	42.5	1.3	49
Cleaned smooth			17.2	1.3	55
As-received smooth	300		57.6	1.9	52
As-received rough	200		65.5	11.6	47
Cleaned rough			35.4	5.1	56

Contact angle for the cleaned smooth wafer (wafer diameter = 165 mm) decreased from a mean value of 42.5° to 17.2° with an average standard deviation of ±1.3° while the contact angle of cleaned rough wafer (wafer diameter = 200 mm) decreased from a mean value of 65.5° to 35.4° with an average standard deviation of ±5.1°. The surface roughness underwent no/minimal change based on the fact that the standard deviations showed identical behavior as in the case of "as-received" smooth and rough silicon wafers.

4.6. Atomic Force Microscopy (AFM)

Atomic force microscopy (AFM) is a microscopic technique that can image three-dimensional topography of the surface at atomic resolution. A cantilever with a sharp tip probes the surface. Depending on mode of scanning, the technique can provide high resolution topographic images. The three types of modes are (i) Contact mode, (ii) Non-contact mode and (iii) Tapping mode.

Tapping mode AFM is a key advance in AFM. This potent technique allows high resolution topographic imaging of sample surfaces that are easily damaged, or difficult to image by other AFM techniques. Tapping mode overcomes problems associated with friction, adhesion, electrostatic forces, and other difficulties that an plague conventional AFM scanning methods by alternately placing the tip in contact with the surface to provide high resolution and then lifting the tip off the surface to avoid dragging the tip across the surface. Tapping mode imaging is implemented in ambient air by oscillating the cantilever assembly at or near the cantilever's resonant frequency using a piezoelectric crystal. The piezo motion causes the cantilever to oscillate with a high amplitude when the tip is not in contact with the surface. The oscillating tip is then moved toward the surface until it begins to lightly touch, or tap the surface. During scanning, the vertically oscillating tip alternately contacts the surface and lifts off. As the oscillating cantilever begins to intermittently contact the surface, the cantilever oscillation is necessarily reduced due to energy loss caused by the tip contacting the surface. The reduction in oscillation amplitude is used to identify and measure surface features. When the tip passes over a bump in the surface, the cantilever has less room to oscillate and the amplitude of oscillation decreases. Conversely, when the tip passes over a depression, the cantilever has more room to oscillate and the amplitude increases. The oscillation amplitude of the tip is measured by the detector and input to controller electronics. The digital feedback loop then adjusts the tip-sample separation to maintain a constant amplitude and force on the sample.

Tapping mode AFM (Veeco di Innova) was used to characterize “as-received” and RCA cleaned smooth silicon wafer. A scan area of 10 μm x 10 μm, 5 μm x 5 μm and

1 µm x 1 µm was chosen at two locations on these surfaces. Scan results are shown in Figures 57 through 62 and summarized in Table 3.

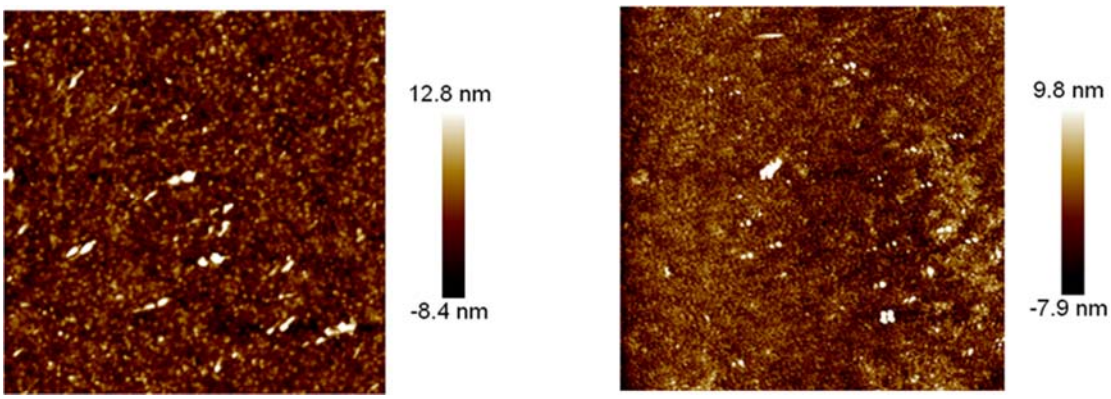

Figure 57: AFM images of "as-received" 165 mm smooth silicon wafer at locations 1 and 2 for a scan area of 10 µm x 10 µm.

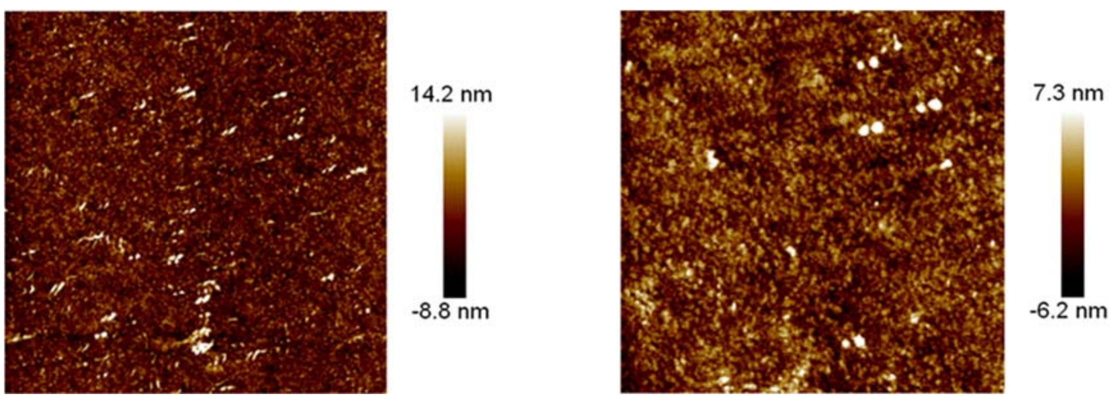

Figure 58: AFM images of "as-received" 165 mm smooth silicon wafer at locations 1 and 2 for a scan area of 5 µm x 5 µm.

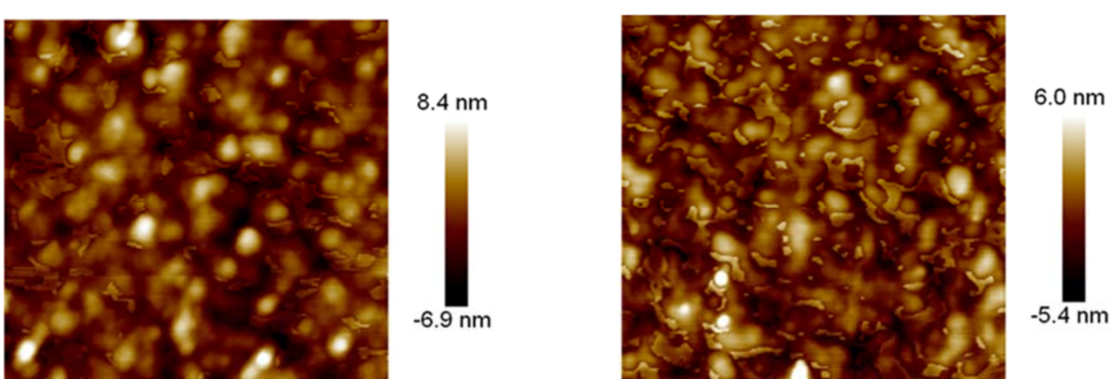

Figure 59: AFM images of "as-received" 165 mm smooth silicon wafer at locations 1 and 2 for a scan area of 1 µm x 1 µm.

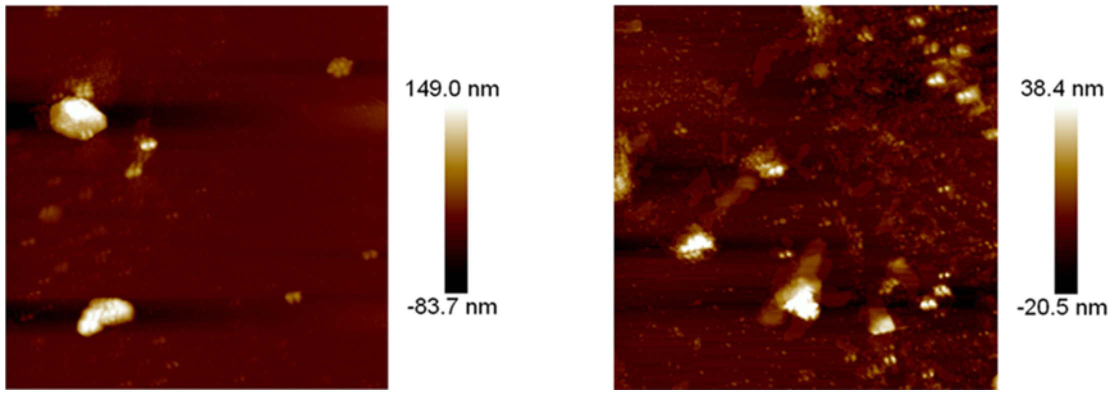

Figure 60: AFM images of cleaned 165 mm smooth silicon wafer at locations 1 and 2 for a scan area of 10 µm x 10 µm.

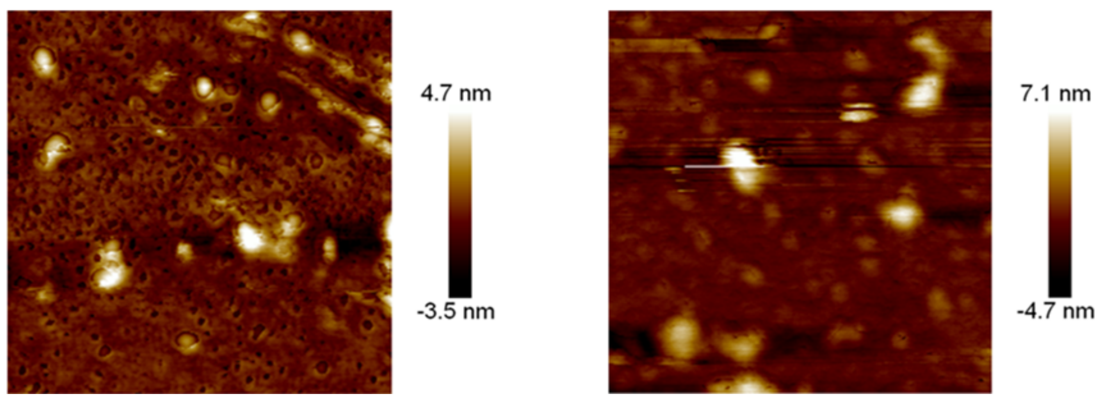

Figure 61: AFM images of cleaned 165 mm smooth silicon wafer at locations 1 and 2 for a scan area of 5 µm x 5 µm.

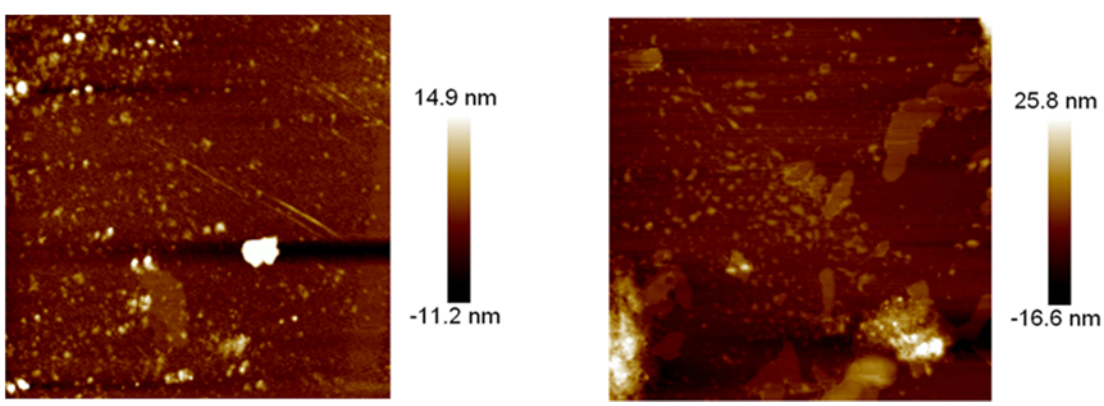

Figure 62: AFM images of cleaned 165 mm smooth silicon wafer at locations 1 and 2 for a scan area of 1 µm x 1 µm.

Table 3: Mean squared average of surface roughness for smooth silicon wafer.

Smooth silicon wafer Diameter = 165 mm		10 μm x 10 μm	5 μm x 5 μm	1 μm x 1 μm	Units
As-received	Location 1	2.36	2.3	1.82	nm
	Location 2	1.71	1.72	1.38	nm
Cleaned	Location 1	1.57	1.23	0.71	nm
	Location 2	1.98	2.05	0.541	nm

The results indicate that the surface roughness is of the order of nanometers and the etching of surface using RCA process does not indicate change in the surface roughness. These results were inconclusive due to surface roughness nearing the instrument detection limits. These results coupled with contact angle indicate change in surface chemistry.

4.7. Water impingement on vertically oriented spinning cleaned silicon wafer

4.7.1. Rotation of cleaned 200 mm rough silicon wafer

Rotation of cleaned 200 mm rough silicon wafer exhibited dynamics identical to the "as-received" rough silicon wafer. The impingement of water on this surface while being rotated exhibited eddies, secondary hydraulic jump and the ripples at the hydraulic jump lip.

The phenomena appeared at rotational speeds close to the phenomena observed on "as-received" rough silicon wafer suggesting that the contact angle did not affect the appearance and disappearance of these observed phenomena when subjected to identical conditions.

The image matrices in Figures 63 and 64 summarize various transitions captured at different rotational speeds of the wafer. All of these transitions were observed for flow rates used in this experiment. Figure 65 also includes disappearance of hydraulic jump at specified rotational rate. The timescale for the hydraulic jump disappearance was observed to be less than 5 seconds.

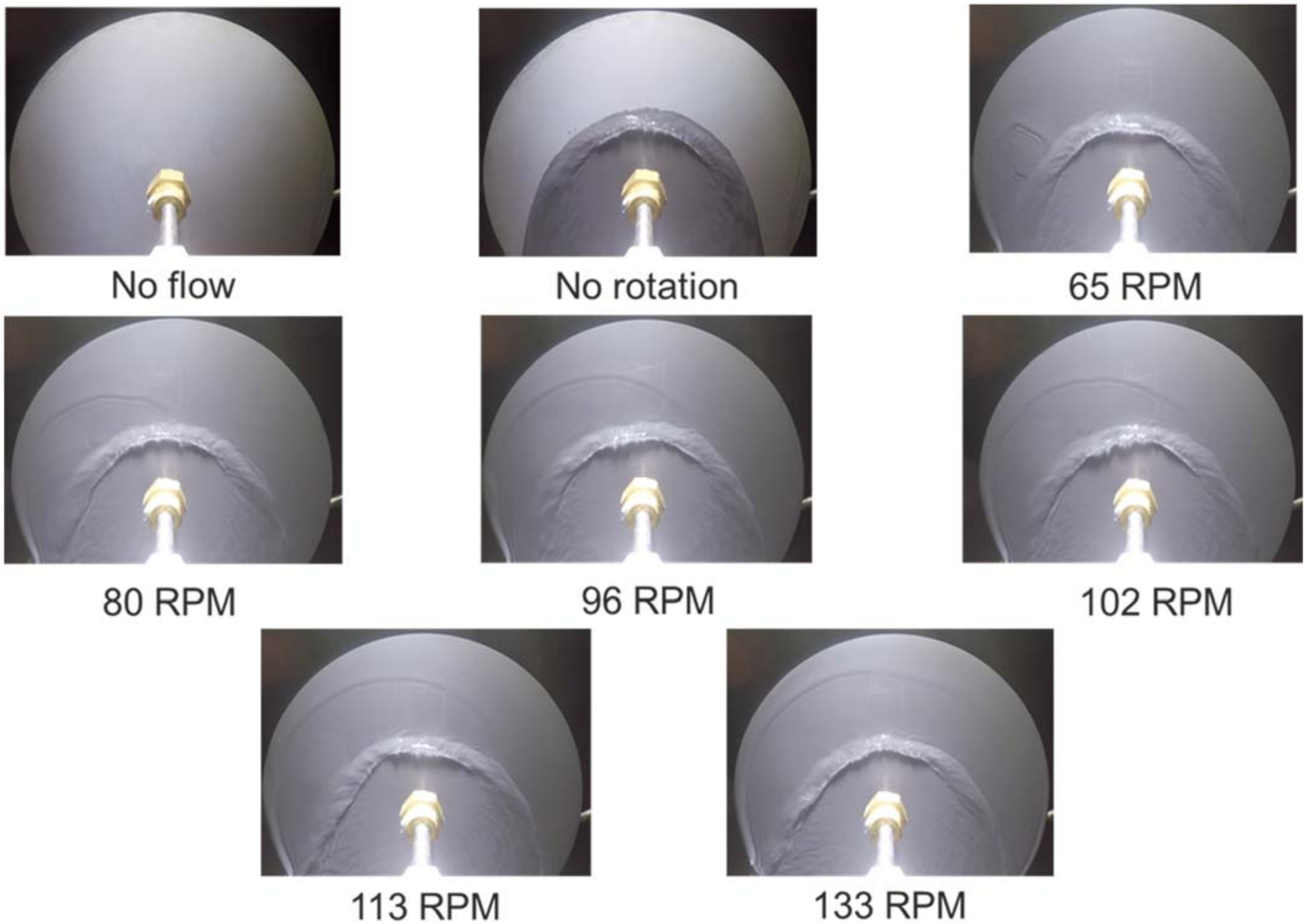

Figure 63: Image matrix (part-1) for a cleaned 200 mm rough silicon wafer at different rotational speeds when impinging coherent water jet at a flowrate of 0.4 USGPM.

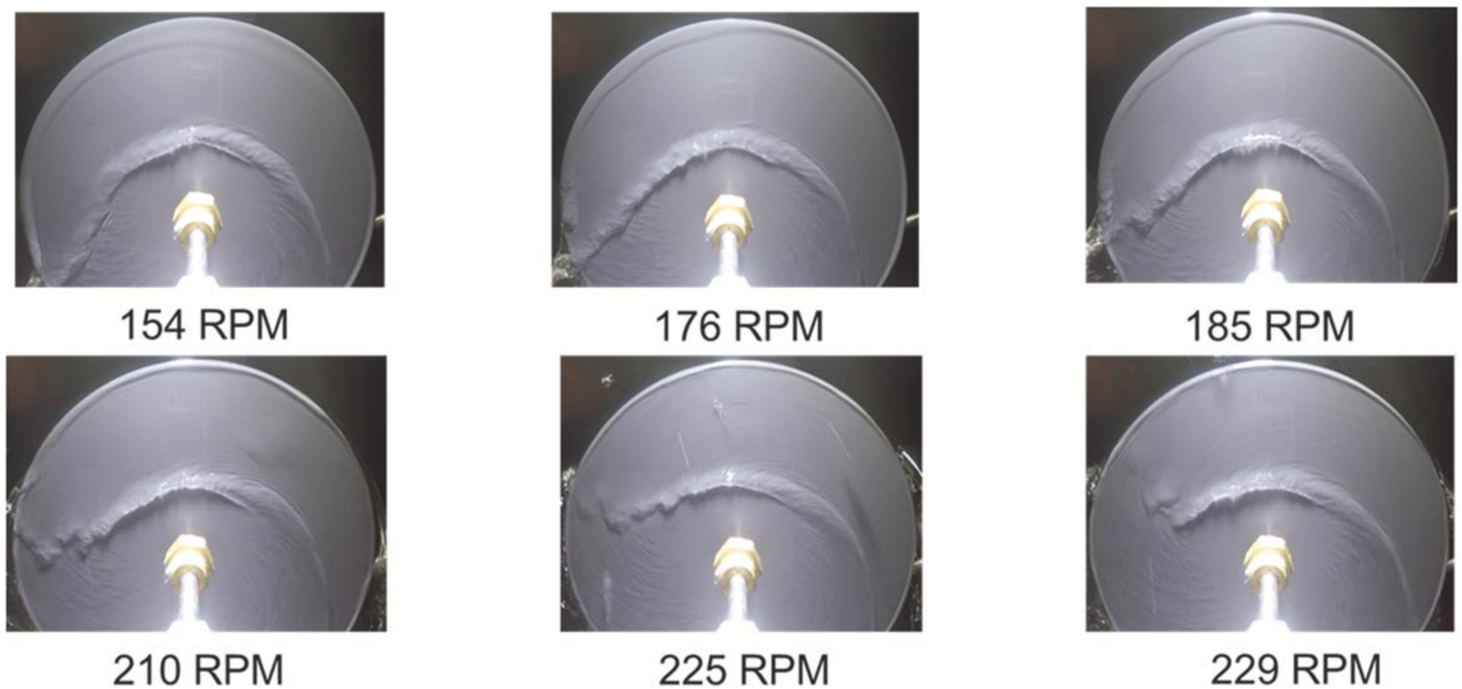

Figure 64: Image matrix (part-2) for a cleaned 200 mm rough silicon wafer at different rotational speeds when impinging coherent water jet at a flowrate of 0.4 USGPM.

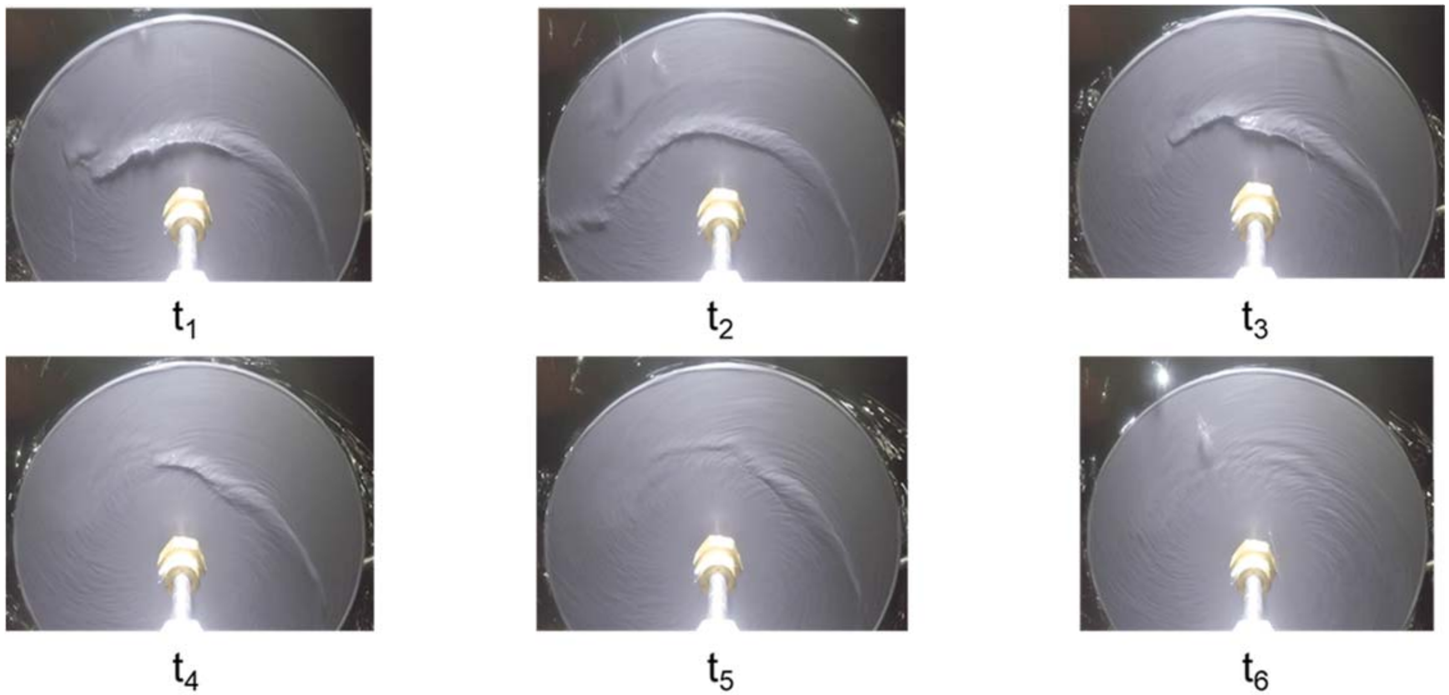

Figure 65: Disappearance of hydraulic jump for a cleaned 200 mm rough silicon wafer at 229 RPM when impinging coherent water jet at a flowrate of 0.4 USGPM. The time-scale ($t_1 \rightarrow t_6$) at critical rotational speed for disappearance of hydraulic jump is bracketed between 3 – 5 seconds.

4.7.2. Rotation of cleaned 165 mm smooth silicon wafer

Rotation of cleaned 165 mm smooth silicon wafer exhibited dynamics identical to the "as-received" rough silicon wafer (Figures 27 and 28) and cleaned 200 mm rough silicon wafer (Figures 63 and 64). The impingement of water on this surface while being rotated exhibited eddies, secondary hydraulic jump and the ripples at the hydraulic jump lip.

The phenomena could be seen below water flowrate of 0.3 USGPM suggesting dependence of wafer diameter on the observed phenomena. No "stick-slip" phenomena was observed on this surface suggesting that the change in surface behavior was successfully achieved by the RCA process. The critical rotational speed was observed to be close to the critical rotational speed of the "as-received" 165 mm smooth silicon wafer.

The image matrices in Figures 66 and 67 summarize various transitions captured at different rotational speed of the wafer. All of these transitions were observed for flow rates under 0.3 USGPM used in this experiment. Figure 67 also includes disappearance of hydraulic jump at specified rotational rate. The timescale for the hydraulic jump disappearance was observed to be less than 5 seconds.

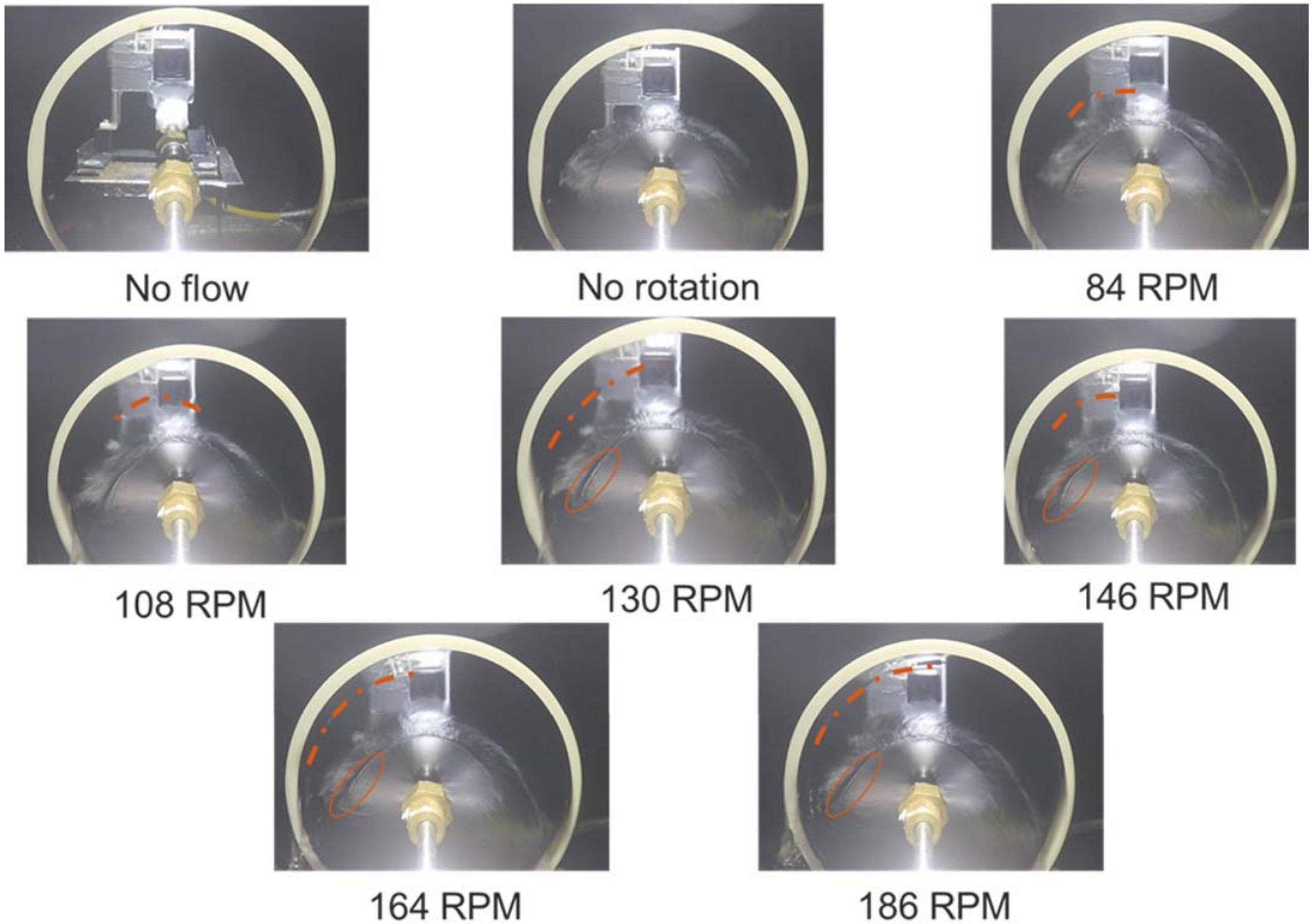

Figure 66: Image matrix (part-1) for a cleaned 165 mm smooth silicon wafer at different rotational speeds when impinging coherent water jet at a flowrate of 0.3 USGPM.

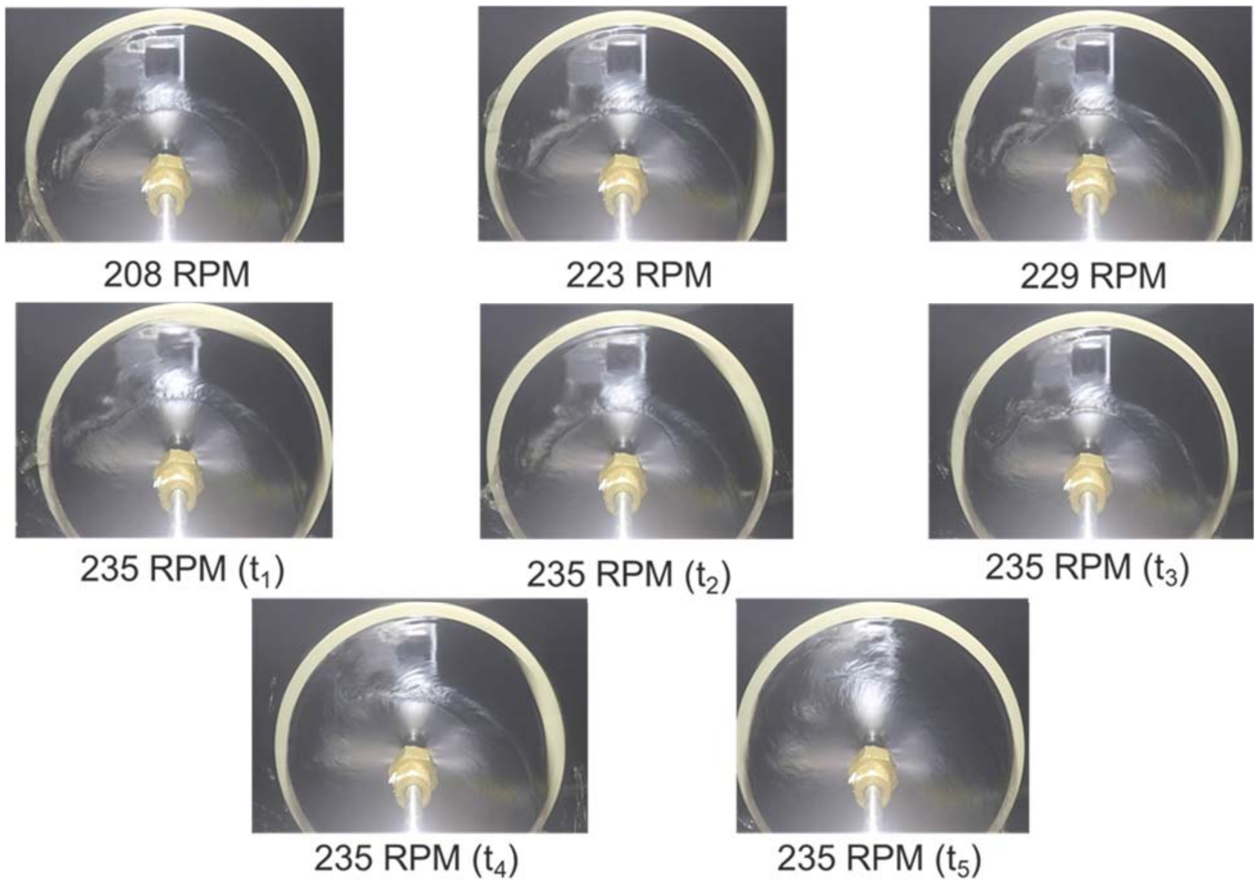

Figure 67: Image matrix (part-2) and hydraulic jump disappearance for a cleaned 165 smooth silicon wafer at different rotational speeds when impinging coherent water jet at a flowrate of 0.3 USGPM. The time-scale ($t_1 \rightarrow t_6$) at critical rotational speed for disappearance of hydraulic jump is bracketed between 3 seconds to 5 seconds.

4.8. Wafer draining test

A draining test on all vertically oriented wafers was performed to understand the wetting behavior of water on these surfaces. The spinning wafers were impinged with water till the hydraulic jump disappeared. The water impingement and the wafer spinning were abruptly stopped and the draining of water on the wafer surface was observed.

"As-received" and cleaned 200 mm rough wafers showed similar draining and wetting behaviors where the residual water on the surface (under the influence of gravity) drained immediately but the wafer remained wet due to the surface roughness.

"As-received" 165 mm smooth wafer showed an immediate water pullback effect where the coherence force of water is greater than the fluid/surface interaction energy. This solidifies the point of smooth wafer having poor wettability due to low surface energy, thus, exhibiting slip-stick phenomena even though the static contact angle measurements are lower than that of the rough wafers (that apparently show better wetting behavior due to higher surface roughness).

Cleaned 165 mm smooth wafer showed wetting and draining behaviors similar to the rough wafer surfaces. In this case, better wetting is achieved by changing the surface energy of the smooth silicon wafer (that was successfully confirmed by contact angle measurements as tabulated in Table 2).

"As-received" 300 mm smooth wafer showed an interesting behavior where the wafer initially shows good wetting, but, with an extended timescale for draining, shows pullback effect as the coherent force of water overcomes the surface energy of this wafer. Studying the hydraulic jump dynamics on a "RCA cleaned" 300 mm smooth wafer is relegated to future work.

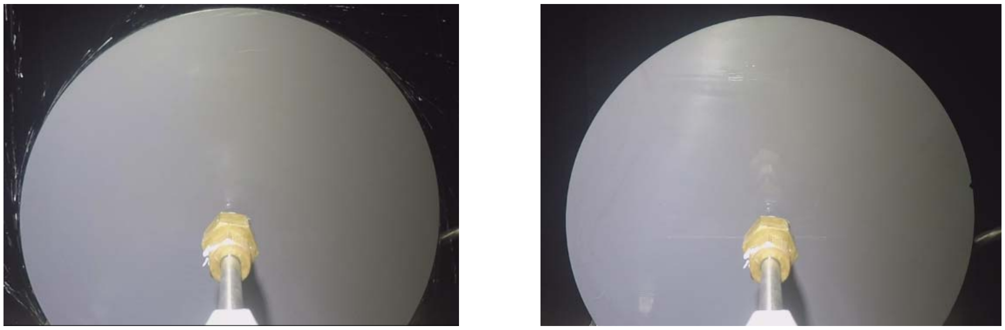

L **R**

Figure 68: "Cleaned" 200 mm rough wafer (L) rotation and (R) draining.

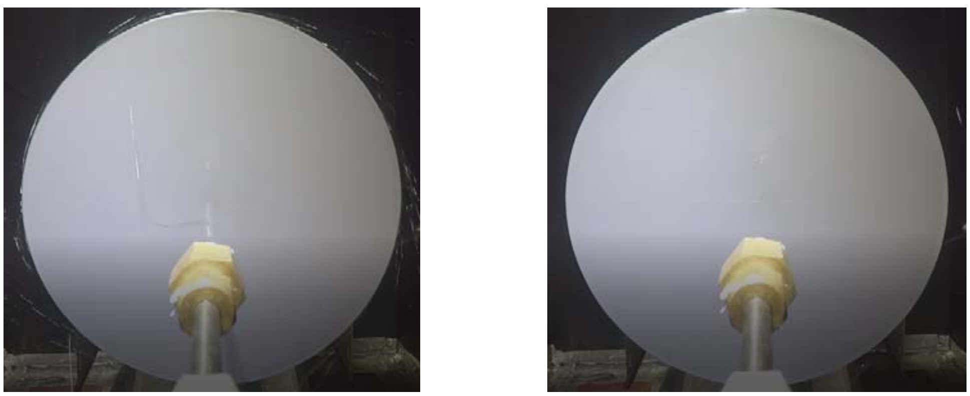

L **R**

Figure 69: "As-received" 200 mm rough wafer (L) rotation and (R) draining.

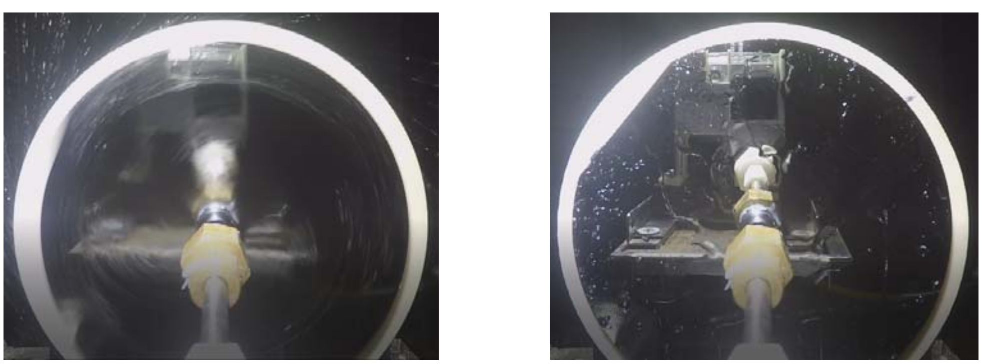

L **R**

Figure 70: "As-received" 165 mm smooth wafer (L) rotation and (R) draining.

L R

Figure 71: "Cleaned" 165 mm smooth wafer (L) rotation and (R) draining.

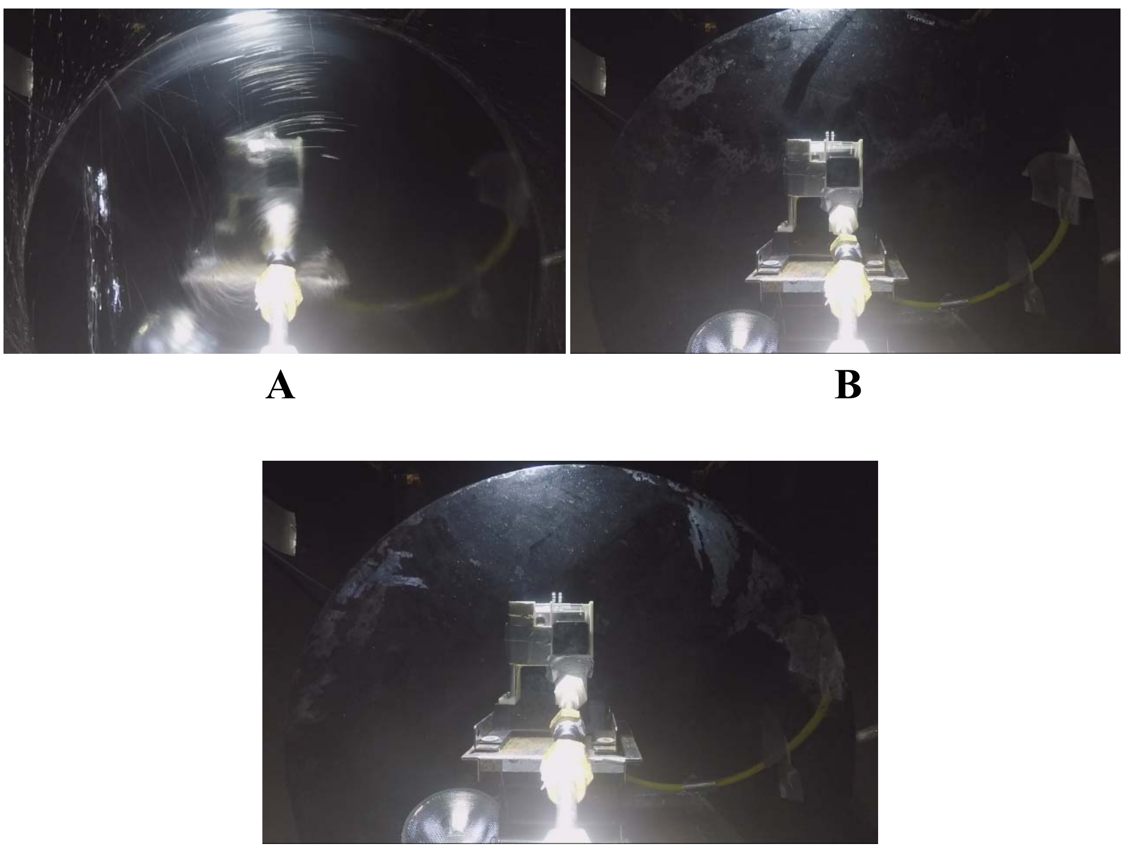

A B

C

Figure 72: "As-received" 300 mm silicon wafer (A) rotation, (B) draining at t = 0 second after stopping the impingement and rotation and (C) water pullback at t = 2 seconds after stoppingthe impingement and rotation.

4.9. Phase Diagram

A phase diagram is a pictorial representation of thresholds where change in behavior of a dynamic event occurs. Disappearance of the hydraulic jump is one such event when involving rotation of vertically oriented wafer being impinged with coherent jet. When the wafer was rotated at fast enough speeds (i.e. critical rotational speeds), the hydraulic jump disappeared as the centrifugal force could overcome the resultant force (gravitational force and momentum force) that led to the formation of hydraulic jump. A relationship between rotational speed and jet velocity is developed for different surfaces after studying five surfaces with different surface characteristics. Such a relationship is developed between Strouhal number (St) that accounts for the frequency of rotation and the jet Reynolds number (Re) that accounts for the fluid properties and the jet velocity.

Strouhal number (St) is a dimensionless number describing oscillating flow mechanisms.

$$St = \frac{fL}{U}$$

where f is the frequency of wafer rotation, L is the characteristic length and U is the flow velocity.

Reynolds number (Re) is a dimensionless number relating the inertial force to the viscous force in a fluid.

$$Re = \frac{DU\rho}{\mu}$$

where D is the characteristic diameter, U is the flow velocity, ρ is the fluid density and μ is the fluid viscosity.

Figure 73 is a phase diagram that shows disappearance of hydraulic jump for surfaces with different characteristics. The Strouhal number on the y-axis includes rotational frequency of the wafer [s^{-1}], jet diameter as the characteristic length [m], and jet velocity as the flow velocity [$m.s^{-1}$]. The Reynolds number on the x-axis includes jet diameter [m], jet velocity [$m.s^{-1}$], density of water [$kg.m^{-3}$] at 20°C and viscosity of water [$kg.m^{-1}.s^{-1}$] at 20°C.

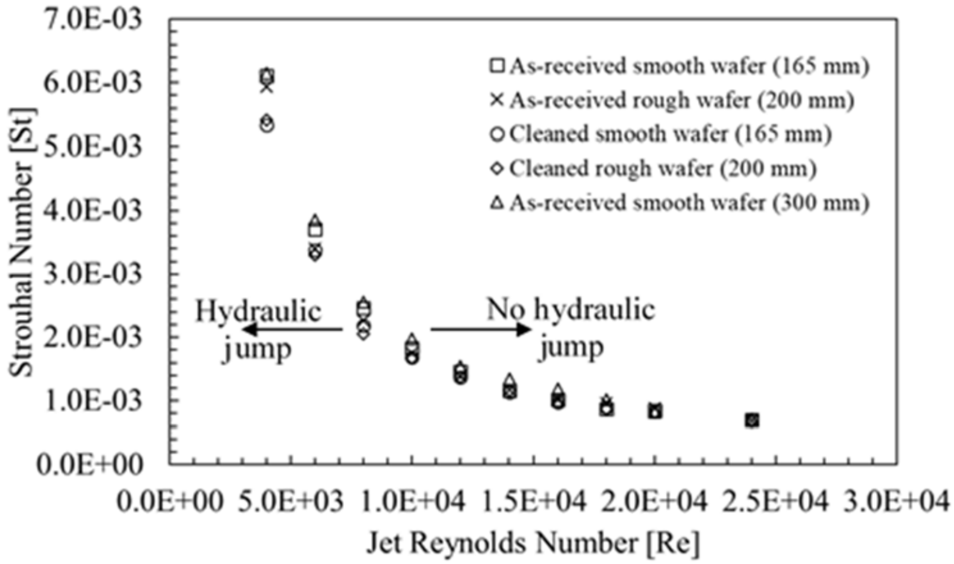

Figure 73: The phase diagram relating the critical rotational speed of wafer to the jet velocity for all wafers irrespective of surface finish or size.

The phase diagram indicates that at critical rotational speeds, the disappearance of hydraulic jump is independent of the surface behavior or fluid-surface interactions. The diagram is developed for a Newtonian coherent water jet for which the jet diameter can be safely assumed to be the nozzle diameter.

5. Discussion and Future Work

The experimental results related to the stationary hydraulic jump presented in this study using the constructed apparatus provide data which is consistent with those of previous researchers. This conclusion is based on the fact that these stationary hydraulic jump dimensions were successfully obtained for the "as-received" 200 mm rough silicon wafer and a trend similar to the PMMA and glass surfaces reported by Wang et al (2013). Those researchers concluded that the hydraulic jump locations were sensitive to the type of surfaces at low flow rates (< 0.175 USGPM) but were insensitive at higher flow rates. Similar observations were made in the present studies for a singular point at low flow rate. One possible explanation could be that this is due to the jet slack at relatively low flowrates resulting in a non-perpendicular impingement of water jet on the surface. The results in Figures 11 - 14 also suggest that the hydraulic jump dimensions versus jet velocity drop off from the linear relationship at low flow rates. It is speculated that the shift in the location of hydraulic jump may be due to the non-perpendicular impingement of the coherent water jet (jet slack).

The phenomenological observations during rotation of surfaces clearly suggest that the surface type affects the dynamics observed around the hydraulic jump at speeds below critical rotational speeds (as indicated by the previously presented image matrices for different surfaces). Phenomena like eddies, secondary hydraulic jumps and ripples were observed on the "as-received" 200 mm rough wafer and the cleaned 200 mm rough wafer. Such phenomena were also observed for the cleaned 165 mm smooth silicon wafer. 200 mm rough surfaces (as-received and cleaned) exhibit relatively high contact angles. 165 mm smooth as-received surface has relatively low contact angles (refer Table 2). The "as-received" 165 mm smooth silicon wafer exhibits slip-stick phenomena due to the fluid/substrate interaction. Contact angle measurements were also performed on these surfaces with SDS solution (40 dynes/cm versus water at 72.8 dynes/cm) but due to high wetting on all of these surfaces, accurate contact angle measurements could not be obtained (but appeared to be less than 5°. Studying the impingement of a fluid with low surface tension under experimental conditions describe in Section 3 on this surface could help explore the impact that surface tension has on the dynamics associated with hydraulic jump in rotating surfaces.

The eddies and secondary hydraulic jump disappear on the cleaned 165 mm smooth silicon wafer at flowrates greater than 0.3 USGPM indicating that these phenomena move out of the frame of the wafer due to the difference in diameters of the wafers used in this study. Thus, the wafer diameter has an influence in the existence of these phenomena. The "as-received" 300 mm smooth silicon wafer exhibited behaviors identical to the "as-received" 200 mm rough silicon wafer. A study involving rotation of the 300 mm smooth wafer at higher impinging flowrates would help in indicating the presence / absence of eddies and secondary hydraulic jump at higher flowrates, thus, solidifying the dependence of these phenomena on the diameter of the substrates that are rotated. Ripples that were observed along the right lip of the hydraulic jump (during clockwise rotation of surface) were apparently dependent on the jet velocity because the ripples remained at higher rotational speeds as the flowrates increased. Such a dependence is not straightforward as the surface type may also play a role in the appearance of these ripples.

The phase diagram is a convenient way to visualize the phenomenological dynamics associated with the hydraulic jump. The phase diagram developed for different surfaces as presented in Figure 73 suggests that irrespective of type of the surface, at critical rotational speeds, the relationship between the Strouhal Number and the Reynolds Number is the same for all surfaces. These dimensionless numbers successfully tie the frequency of wafer rotation to the fluid velocity for Newtonian fluids. Thus, the Figure 68 depicts distinct regions that can predict the appearance and disappearance of the hydraulic jump on vertically oriented rotating surfaces when impinged with coherent Newtonian jets.

Areas of future studies could be

(a) The effect of jet diameter on the phase diagram of Strouhal Number versus Reynolds Number.
(b) Angle of jet impingement which would allow for more flexibility in industrial applications.

(c) Use of various surface tension fluids which lead to lower contact angles and enhanced surface wettability.

(d) The use of non-Newtonian and viscoelastic fluids which play an important role in industrial applications.

6. Nomenclature

$\mathbf{R^i_{\perp}}$ – *inner* radius of the jump perpendicular to gravity at mid-plane

$\mathbf{R^o_{\perp}}$ – *outer* radius of the jump perpendicular to gravity at mid-plane

$\mathbf{R^i_{\parallel}}$ – *inner* height of the jump parallel to gravity

$\mathbf{R^o_{\parallel}}$ – *outer* height of the jump parallel to gravity

$\Delta\mathbf{R}_{\perp}$ – the rope width at mid-plane

$\Delta\mathbf{R}_{\parallel}$ – the rope width at the top of the jump

$\mathbf{n_D}$ – the jet diameter or the nozzle diameter

g – acceleration due to gravity

O – jet impingement point

D – silicon wafer diameter

Re – jet Reynolds number

RPM – rotations per minute

V – Voltage

St – Strouhal number

RCA – Radio Corporation of America

AFM – Atomic Force Microscopy

f – frequency of rotation

U – jet velocity

$\boldsymbol{\rho}$ – fluid density

$\boldsymbol{\mu}$ – fluid viscosity

$\boldsymbol{\gamma}$ – fluid surface tension

7. References

Rayleigh, L. (1914). On the Theory of Long Waves and Bores. Proceedings of the Royal Society of London. Series A, Containing Papers of a Mathematical and Physical Character (1905-1934), 90(619), 324-328.

Tani, I. (1949). Water Jump in the Boundary Layer. Journal of the Physical Society of Japan, 4(4-6), 212-215.

Watson, E. (1964). The radial spread of a liquid jet over a horizontal plane. Journal of Fluid Mechanics, 20(3), 481-499.

R. G. Olsson, & E. T. Turkdogan. (1966). Radial Spread of a Liquid Stream on a Horizontal Plate. Nature, 211(5051), 813-816.

Morison, & Thorpe. (2002). Liquid Distribution from Cleaning-in-Place Sprayballs. Food and Bioproducts Processing, 80(4), 270-275.

Bush, J., & Aristoff, J. (2003). The influence of surface tension on the circular hydraulic jump. Journal of Fluid Mechanics, 489(489), 229-238.

Gennes, P., Brochard-Wyart, Quéré, & Springerlink. (2004). Capillarity and Wetting Phenomena: Drops, Bubbles, Pearls, Waves. New York, NY: Springer New York.

Bush, J., Aristoff, J., & Hosoi, A. (2006). An experimental investigation of the stability of the circular hydraulic jump. Journal of Fluid Mechanics, 558, 33-52.

Kibar, A., Karabay, H., Yiğit, K., Ucar, S., & Erbil, I. (2010). Experimental investigation of inclined liquid water jet flow onto vertically located superhydrophobic surfaces. Experiments in Fluids, 49(5), 1135-1145.

Wilson, Le, Dao, Lai, Morison, & Davidson. (2012). Surface flow and drainage films created by horizontal impinging liquid jets. Chemical Engineering Science, 68(1), 449-460.

Wang, Faria, Stevens, Tan, Davidson, & Wilson. (2013). Flow patterns and draining films created by horizontal and inclined coherent water jets impinging on vertical walls. Chemical Engineering Science, 102(C), 585-601.

Yuan Y., Lee T.R. (2013) Contact Angle and Wetting Properties. In: Bracco G., Holst B. (eds) Surface Science Techniques. Springer Series in Surface Sciences, vol 51. Springer, Berlin, Heidelberg

Walker, T., Hsu, Fitzgibbon, Frank, Mui, Zhu, Fuller. (2014). Enhanced particle removal using viscoelastic fluids. Journal of Rheology, 58(1), 63-88.

Bhagat, & Wilson. (2016). Flow in the thin film created by a coherent turbulent water jet impinging on a vertical wall. Chemical Engineering Science, 152, 606-623.

Glover, Brass, Bhagat, Davidson, Pratt, & Wilson. (2016). Cleaning of complex soil layers on vertical walls by fixed and moving impinging liquid jets. Journal of Food Engineering, 178(C), 95-109.

Bhagat, Perera, & Wilson. (2017). Cleaning vessel walls by moving water jets: Simple models and supporting experiments. Food and Bioproducts Processing, 102, 31-54.

Wang, Y., & Khayat, R. (2018). Impinging jet flow and hydraulic jump on a rotating disk. Journal Of Fluid Mechanics, 839, 525-560.

(n.d.). Retrieved from http://www.chembio.uoguelph.ca/educmat/chm729/afm/ detai-ls .htm

Appendix A

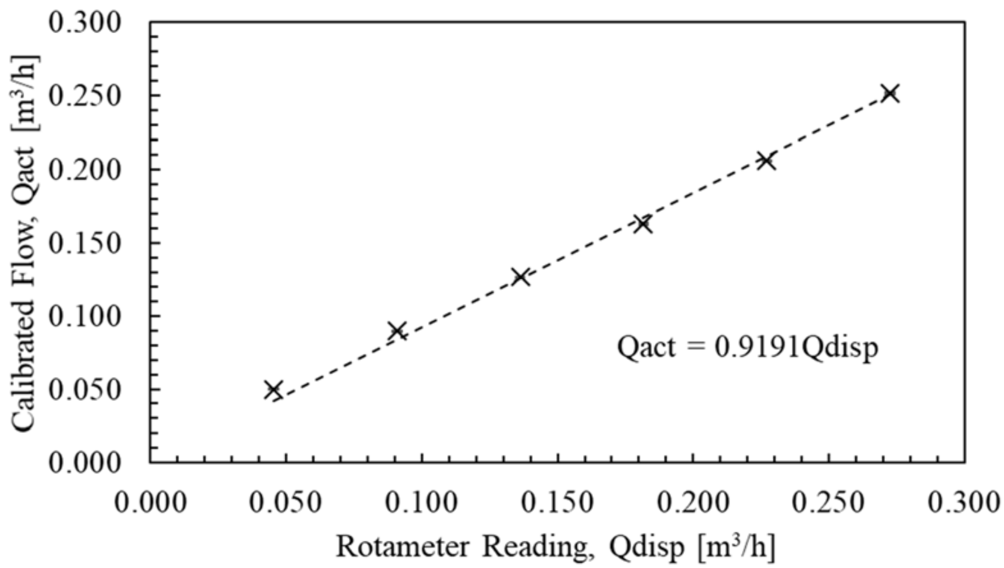

Figure 74: CalQFlo Rotameter calibration.

Figure 74 is a calibration curve for the rotameter installed in this setup. The plot was developed for 3 trials over the operated flow range and the maximum standard deviation observed was ± 0.001 m^3/h.

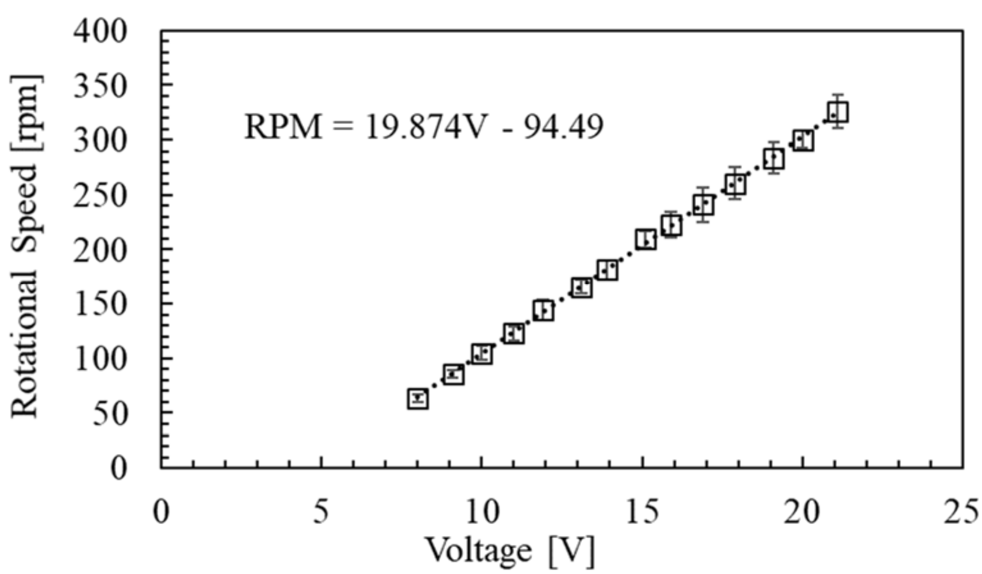

Figure 75: Rotational speed calibration for a smooth silicon wafer (D = 165 mm) with respect to the voltage of the drive.

As indicated in Figure 75, a linear trend relating rotational speed to voltage is observed for the 165 mm smooth silicon wafer. Maximum standard deviation of 16 RPM was observed at the voltage setting of 16.9 Volts. An average standard deviation of 9.4 RPM was observed.

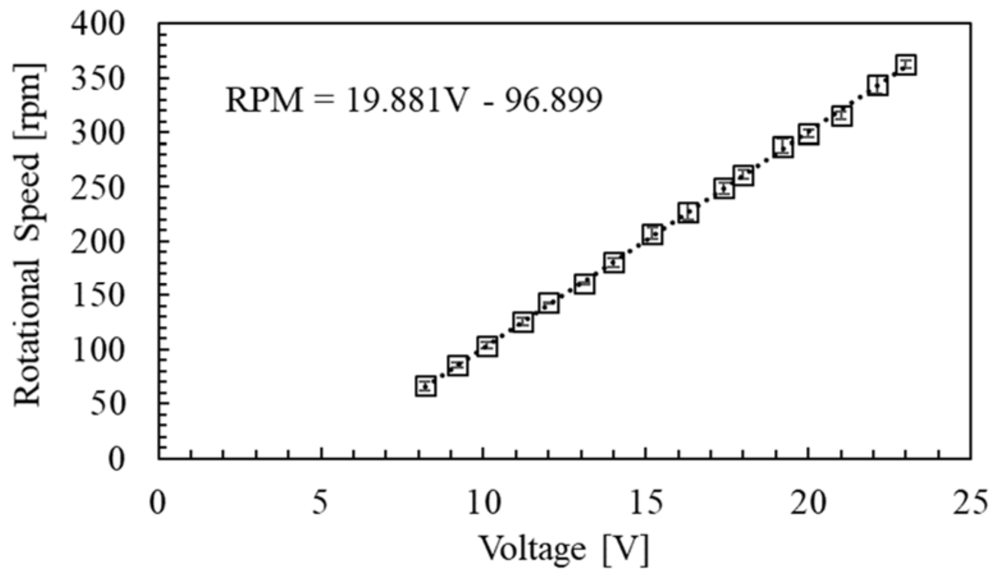

Figure 76: Rotational speed calibration for a rough silicon wafer (D = 200 mm) with respect to the voltage of the drive.

As indicated in Figure 76, a linear trend relating rotational speed to voltage is observed for the 200 mm rough silicon wafer. Maximum standard deviation of 8.4 RPM was observed at the voltage setting of 22.1 Volts. An average standard deviation of 4.2 RPM was observed.

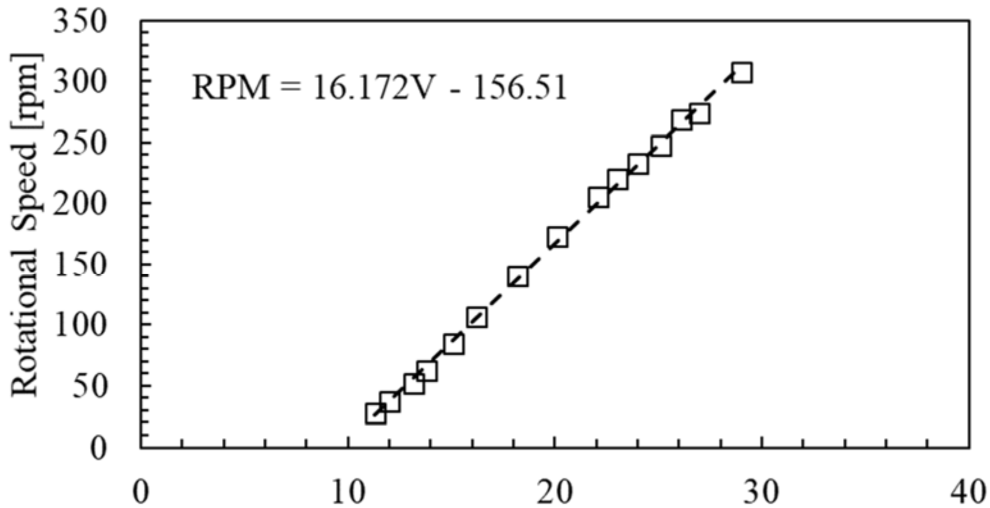

Figure 77: Rotational speed calibration for a smooth silicon wafer (D = 300 mm) with respect to the voltage of the drive.

Appendix B

MATLAB® Code

Average Image Script

```
close all
clc
clear all

[baseFileName, folderName, FilterIndex] = uigetfile('*.mov');

AverageImageName=input('input file name of form: Concentration_Flowrate_AverageImage
','s');

[high_contrast,pixel_length,bw,avg]=AverageImage(baseFileName, folderName, FilterIndex);

save(AverageImageName)
```

Image Analysis

```
close all
clc
clear all

%[FileName, FolderName, FILTERINDEX] = uigetfile('*.mat');

SampleName=input('Enter Sample Name in format D_Fluid_Flowrate: ','s');
PictureName=input('Enter Picture Name in format I_Fluid_Flowrate: ','s');
load('H_02GPM_Water')
figure
imshow(avg)
set(gca,'YDir','normal')

%User defines the impingement point by selecting three points:
```

```
%Left side of impingement
%Right side of impingement
%Top of the impingement

[impingementleftx,impingementlefty]=ginput(1);
referenceline=refline(0,impingementlefty);
[impingementrightx,impingementrighty]=ginput(1);

[impingementtopx,impingementtopy]=ginput(1);
%Defines the center point of the impingement point, generates a circle
%around the point of impingement to check accuracy of point selection

impingementradius=abs(impingementrightx-impingementleftx)/2;
impingementcenterx=impingementleftx+impingementradius;
impingementcentery=impingementtopy-impingementradius;

origin=[impingementcenterx,impingementcentery];
vertline=line([impingementcenterx,impingementcenterx],[0,1080]);

impingementcircle=viscircles(origin,impingementradius);

%Plots line at various angles - PJ
lineLength = 1080;
% angle1=15;
% x1(1) = impingementcenterx;
% y1(1) = impingementcentery;
% x1(2) = x1(1) + lineLength * cosd(angle1);
% y1(2) = y1(1) + lineLength * sind(angle1);
% hold on;
% plot(x1, y1);

angle2=30;
x2(1) = impingementcenterx;
y2(1) = impingementcentery;
x2(2) = x2(1) + lineLength * cosd(angle2);
y2(2) = y2(1) + lineLength * sind(angle2);
hold on;
```

```
plot(x2, y2);

% angle3=45;
% x3(1) = impingementcenterx;
% y3(1) = impingementcentery;
% x3(2) = x3(1) + lineLength * cosd(angle3);
% y3(2) = y3(1) + lineLength * sind(angle3);
% hold on;
% plot(x3, y3);

angle4=60;
x4(1) = impingementcenterx;
y4(1) = impingementcentery;
x4(2) = x4(1) + lineLength * cosd(angle4);
y4(2) = y4(1) + lineLength * sind(angle4);
hold on;
plot(x4, y4);

% angle5=75;
% x5(1) = impingementcenterx;
% y5(1) = impingementcentery;
% x5(2) = x5(1) + lineLength * cosd(angle5);
% y5(2) = y5(1) + lineLength * sind(angle5);
% hold on;
% plot(x5, y5);

%Ends here - PJ

%Generates a reference line to help define y coordinates at the edges of
%the jump

r = refline(0,origin(2)); %Reference line through center
set(r,'LineWidth',1);

hold on

%User selects top of jump (R_Parallel_Inner).
```

```
[jumptopx,jumptopy]=ginput(1);

%Plots the points as dots for checking error
plot(jumptopx,jumptopy,'r.','MarkerSize',20);

%User selects top of jump (R_Parallel_Outer) - PJ
[jumptopx2,jumptopy2]=ginput(1);
%Plots the points as dots for checking error - PJ
plot(jumptopx2,jumptopy2,'r.','MarkerSize',20);

%User selects left and right of jump
[jumpsidex,jumpsidey]=ginput(2);

plot(jumpsidex,jumpsidey,'g.','MarkerSize',20);

%User selects left and right of rope
[rcx,rcy]=ginput(2);
plot(rcx,rcy,'c.','MarkerSize',20)

%User selects 20 points to define the jump
[jumppointsx,jumppointsy]=ginput(20);
plot(jumppointsx,jumppointsy,'m.','MarkerSize',20)

%Curve fitting over user selected points - PJ
txy = polyfit(jumppointsx,jumppointsy,2);
tx1 = linspace(-1080,1080);
ty1 = polyval(txy,tx1,'o');
plot(tx1,ty1)
%Ends here - PJ

%User selects R_Perpendicular_Inner at various angles (from 15 to 75) - PJ
%[jumpR15x,jumpR15y]=ginput(1);
%plot(jumpR15x,jumpR15y,'k.','MarkerSize',20)
[jumpR30x,jumpR30y]=ginput(1);
plot(jumpR30x,jumpR30y,'k.','MarkerSize',20)
%[jumpR45x,jumpR45y]=ginput(1);
%plot(jumpR45x,jumpR45y,'k.','MarkerSize',20)
```

```
[jumpR60x,jumpR60y]=ginput(1);
plot(jumpR60x,jumpR60y,'k.','MarkerSize',20)
%[jumpR75x,jumpR75y]=ginput(1);
%plot(jumpR75x,jumpR75y,'k.','MarkerSize',20)
%Ends here - PJ

print(PictureName,'-depsc');

hold off

jumpwidth=abs(impingementcenterx-jumpsidex);
averagejumpwidth=(jumpwidth(1)+jumpwidth(2))/2;

jumpheight=abs(jumptopy-impingementcentery);

% Outer Jump height - PJ
jumpheight_outer=abs(jumptopy2-impingementcentery);

%Adjusts the size of the parabola to account for the size of each pixel
Actualheight=jumpheight.*pixel_length
%Height of outer jump (R_Parallel_Outer) - PJ
Actualouterheight=jumpheight_outer.*pixel_length

Actualwidth=averagejumpwidth.*pixel_length

Ratio=Actualheight/Actualwidth;

centeredrcx=abs(rcx-impingementcenterx);
Actualrc=((centeredrcx(1)+centeredrcx(2))/2)*pixel_length
RcRatio=Actualheight/Actualrc;

%Calculates distance from impingement point to inner rope - PJ
%Distance_15deg=sqrtm(((jumpR15x-impingementcenterx).^2)+((jumpR15y-
impingementcentery).^2))*pixel_length
Distance_30deg=sqrtm(((jumpR30x-impingementcenterx).^2)+((jumpR30y-
impingementcentery).^2))*pixel_length
```

```
%Distance_45deg=sqrtm(((jumpR45x-impingementcenterx).^2)+((jumpR45y-
impingementcentery).^2))*pixel_length
Distance_60deg=sqrtm(((jumpR60x-impingementcenterx).^2)+((jumpR60y-
impingementcentery).^2))*pixel_length
%Distance_75deg=sqrtm(((jumpR75x-impingementcenterx).^2)+((jumpR75y-
impingementcentery).^2))*pixel_length
ActualJumppointsx=(jumppointsx-impingementcenterx).*pixel_length;
ActualJumppointsy=(jumppointsy-impingementcentery).*pixel_length;

save(SampleName,'Actualwidth','Actualheight','Actualouterheight','Actualrc','ActualJumppoint
sy','ActualJumppointsx')
```

Average Image

```
function [high_contrast, pixel_length,bw,avg]=AverageImage(baseFileName, folderName,
FilterIndex)

% This program performs the following actions:
% 1. Loads a video file
% 2. Generates the average frame of the video file
% 3. Determines the length of each pixel in the image by measuring the
%    diameter in pixels of a circular reference of known diameter 25.4 mm
% Written by Jason Conradt and Kyle Harris

%1.
clip_title = fullfile(folderName, baseFileName);
video = VideoReader(clip_title);
nf=video.NumberOfFrames;

%Preallocate matrix for the average frame
avg = zeros([video.Height video.Width 3]);



% 2.
% Average RBG pixel magnitudes frame-by-frame and save to a matrix
```

```
% Note: Process takes ~1 min per 3mb of video. Don't get crazy with
% video sizes.
parfor f = 1:nf
  avg = avg + (1/nf).*im2double(read(video,f));
end;

%For the reference
%ref_pic = im2bw(avg,0.12);
%Display image
imshow(avg)
% find black circular reference
[Center,Radius]=imfindcircles(avg,[350 450],'ObjectPolarity','dark','Sensitivity',0.95)
% show the image and draw the detected circles on it
circles=viscircles(Center,Radius)
%Determine the diameter of the reference in pixels
ref=Radius(1)*2;
%Determine the length of each pixel in mm
pixel_length = 200/ref;

% 3.
%Converts image to a binary black and white image.
gray = rgb2gray(avg);
high_contrast = imadjust(gray);
bw = im2bw(high_contrast,.3);

%If multiple circles are detected reducde the sensitivity of imfindcircles
```